University of South Florida
Scholar Commons

Graduate Theses and Dissertations | Graduate School

2010

# Development of UHF micromechanical resonators and arrays based on silicon-on-insulator (SOI) technology

Mingke Xiong
*University of South Florida*

Follow this and additional works at: http://scholarcommons.usf.edu/etd

Part of the American Studies Commons

Scholar Commons Citation
Xiong, Mingke, "Development of UHF micromechanical resonators and arrays based on silicon-on-insulator (SOI) technology" (2010). *Graduate Theses and Dissertations.*
http://scholarcommons.usf.edu/etd/1815

This Thesis is brought to you for free and open access by the Graduate School at Scholar Commons. It has been accepted for inclusion in Graduate Theses and Dissertations by an authorized administrator of Scholar Commons. For more information, please contact scholarcommons@usf.edu.

# Development of UHF Micromechanical Resonators and Arrays Based on Silicon-On-Insulator (SOI) Technology

by

Mingke Xiong

A thesis submitted in partial fulfillment
of the requirements for the degree of
Master of Science in Electrical Engineering
Department of Electrical Engineering
College of Engineering
University of South Florida

Major Professor: Jing Wang, Ph.D.
Andrew M. Hoff, Ph.D
Thomas M. Weller, Ph.D

Date of Approval:
March 20, 2010

Keywords: ALD, capacitive transducer, DRIE, high-k, nano-gap

Copyright© 2010 , Mingke Xiong

To my fiance, my parents, my friends, and my teachers.

**ACKNOWLEDGEMENTS**

I would like to thank the members of my dissertation committee for their always helpful advice and suggestions: Prof. Jing Wang (Chair), Prof. Thomas Weller, and Prof. Andrew Hoff. Without their support, I could not have finished this long journey. I would especially like to thank Prof. Wang for his motivation, guidance, and inspiration throughout the whole master program. Working with him during the past three years has been an extremely valuable and enjoyable experience.

I would also like to thank the former and current students from the group, including Mian Wei, I-Tsang Wu, Cesar Augusto Morales, Julio Mario Dewdney, Kosol Son, Ivan Rivera, Tianpeng Wu, Paula Algarin amaris, Kenza Mouttaki, and Chamila Siyamba.

This thesis work would not be possible without the the constant help and support from Nanomaterial and Nanotechnology Research Center (NNRC): Robert Tufts, Richard Everly, Jay Bieber, Yusuf Emirov, and Sclafani Louis-Jeune.

Most importantly, I would like to thank my fiancé, Ke Sun, my parents, Lan Yu and Chujiang Xiong for their love and support.

## TABLE OF CONTENTS

LIST OF TABLES ……..…….iii

LIST OF FIGURES ..... iv

ABSTRACT ..... vii

CHAPTER 1 INTRODUCTION ..... 1

1.1 Background of Wireless Transceiver Architecture ..... 3
1.1.1 Superheterodyne Architecture ..... 4
1.1.2 Direct Conversion Architecture ..... 5
1.1.3 Architecture Based on RF MEMS Resonator ..... 6
1.2 Macro-scale Vibrating Mechanical Resonator for Wireless Communication ..... 7
1.2.1 Ceramic Device ..... 7
1.2.2 Quartz Crystal Device ..... 8
1.3 Micromechanical Resonators for Wireless Communication ..... 9
1.3.1 Piezoelectrically-Actuated Resonators ..... 11
1.3.1.1 Surface Acoustic Wave (SAW) Resonators ..... 11
1.3.1.2 Bulk Acoustic Wave (BAW) Resonators ..... 12
1.3.2 Capacitively-Transduced MEMS Resonators ..... 16
1.3.2.1 Flexural Mode Beam Resonator ..... 16
1.3.2.2 Radial-Contour Mode Disk Resonator ..... 18
1.3.2.3 Wine-glass Disk Resonator ..... 21
1.3.2.4 Wine-glass Mode Ring Resonator ..... 22
1.3.2.5 Internal Dielectrically-Transduced Bar Resonator ..... 25
1.3.3 Resonator Based on Silicon-on-Insulator (SOI) Technology ..... 26
1.3.3.1 Fabrication on SOI Substrate Utilizing Electron Beam Lithography ..... 27
1.3.3.2 Fabrication on SOI Substrate Utilizing Focus Ion Beam (FIB) Technique ..... 28
1.3.3.3 SOI Fabrication by Conventional Si Micromachining Technique ..... 30
1.4 Resonator Array ..... 34
1.5 Capacitively-Transduced Resonators Using Materials Other than Si ..... 35
1.6 Overview ..... 36

CHAPTER 2 RESONATOR DESIGN ..... 39

2.1 Extensional Wine-glass Mode and Resonance Frequency Design ..... 39
2.1.1 Wine-glass Mode of a Disk Resonator ..... 39
2.1.2 Wine-glass Mode of a Ring Resonator ..... 46
2.2 Equivalent Circuit Model ..... 50

CHAPTER 3 MICROFABRICATION PROCESS OF THE WINE-GLASS MODE DISK RESONATOR AND ARRAY ON SOI SUBSTRATE ..... 56

3.1 Microfabrication Process on SOI Substrate ..... 56
3.2 High-Aspect-Ratio Si DRIE ..... 60
3.2.1 Etch Rate ..... 64
3.2.2 Sidewall Smoothness ..... 66
3.2.3 Aspect Ratio Dependent Etching (ARDE) ..... 67
3.3 Atomic Layer Deposition (ALD) ..... 68

CHAPTER 4 CONCLUSION ..... 73

LIST OF REFERENCES ..... 75

APPENDICES ..... 83

Appendix A: Polysilicon Disk Resonator on SOI Substrate Process Traveler ..... 84

## LIST OF TABLES

Table 1.1 Properties for different materials and their relevant frequencies..... 36
Table 2.1 The related parameter for a disk resonator..... 46
Table 3.1 Different Si DRIE recipe used in this work..... 62
Table 3.2 Precursors, deposition condition and rate of $HfO_2$ deposited by ALD..... 70

## LIST OF FIGURES

Figure 1.1 Simplified architecture of a superheterodyne receiver with single down-conversion. ..... 4

Figure 1.2 Simplified architecture of direct conversion receiver. ..... 5

Figure 1.3 Simplified architecture of RF MEMS resonator-based channel select receiver. ..... 6

Figure 1.4 Mode shapes of quartz crystal unit: (a) contour shear mode; (b) thickness shear mode. ..... 8

Figure 1.5 Schematic of a typical SAW resonator [32]. ..... 11

Figure 1.6 Device implementation for the two types of bulk acoustic wave (BAW) resonators with two different types of acoustic isolation methods [32]: (a) SMR employs Bragg's reflector; and (b) FBAR sits on top of air cavity. ..... 13

Figure 1.7 Contour mode ring resonator [39]: (a) one port circular ring resonator; (b) one port square-shape ring resonator. ..... 14

Figure 1.8 (a) Photo of an AlN dual-mode filter; (b) measured transmission (S21) of the AlN dual-mode filter, along with simulated response based on its equivalent circuit model with different termination impedance [41]. ..... 15

Figure 1.9 Schematic view of different types of beam resonators: (a) cantilever beam resonator; (b) clamped-clamped beam resonator; (c) free-free beam resonator. ..... 17

Figure 1.10 SEM image and measured frequency response in (a) vacuum and (b) air for a polysilicon capacitively-transduced radial-contour mode disk resonator [9]. ..... 18

Figure 1.11 Comparison between (a) a previous disk resonator process; (b) the self-aligned disk resonator process [9]. ..... 19

Figure 1.12 Fabrication process flow of the self-aligned radial-contour mode disk resonator. ..... 21

Figure 1.13 SEM photo and frequency response spectrum in (a) air and (b) vacuum of a polysilicon wine-glass mode disk resonator [51]. ..... 22

Figure 1.14 Perspective-view schematic of the wine-glass mode disk resonator in a typical two-port bias and excitation configuration. ..... 22

Figure 1.15 Perspective-view schematic of the extensional wine-glass ring (EWGR) resonator with typical driving and sensing configuration. ..... 24

Figure 1.16 SEM picture and measured frequency characteristics of a (a) un-notched and (b) notched "hollow disk" EWGR device [53]. ..... 25

Figure 1.17 Picture of a bulk-mode resonator and the measured frequency characteristics at different vibrating mode [10]. ..... 26

Figure 1.18 Fabrication process using e-beam lithography for creating suspended NEMS device on SOI substrate. ..... 28

Figure 1.19 Schematic of the process of MEMS resonator with nano-gap utilizing FIB milling technique: (a) thermal oxide is grown on SOI wafer; (b) photolithography is used to open the release hole; (c) nano-scale gaps are achieved by FIB milling; (d) patterns are transferred to $SiO_2$/Si/$SiO_2$ layers by high aspect-ratio dry etch; (e) metal contacts are patterned by lift-off process after striping the top $SiO_2$ layer; (f) the resonators are released by etching away the buried oxide. ..... 29

Figure 1.20 Bulk lateral resonator with narrow air gap (<100 nm) fabricated by the proposed FIB-based process [62]. ..... 29

Figure 1.21 (a) SEM image and (b) frequency response of an 18 μm-thick wine-glass disk resonator on SOI substrate [55]. ..... 30

Figure 1.22 Fabrication process flow of HARPSS resonator on SOI substrates. ..... 31

Figure 1.23 SEM image of (a) the disk resonator and (b) a zoom-in on the 200 nm gap [66]. ..... 32

Figure 1.24 Fabrication process flow of the TEOS and CMP based method. ..... 33

Figure 1.25 SEM image and frequency response spectra of a single and mechanically coupled square resonator arrays with three and five resonators, respectively [67]. ..... 34

Figure 1.26 Schematic of a 3-by-3 disk resonator array on SOI substrate and its measuring configuration. ..... 38

Figure 2.1 Top view of a wine-glass mode disk resonator. ..... 40

Figure 2.2 Mode shapes and resonance frequency for a 20 μm radius single crystal silicon <100> disk calculated from the theoretical derivation using COMSOL Multiphysics 3.5a with (a) $m = 2$; (b) $m = 3$; (c) $m = 4$; (d) $m = 5$. ..... 45

Figure 2.3 Top view of a wine-glass mode ring resonator. ..... 46

Figure 2.4 The two-port electrical circuit model represented by $Y$-parameters. ..... 50

Figure 2.5 An infinitesimal element $d\theta$ along the circumferential direction $\theta$. ..... 52

Figure 2.6 Electrical equivalent circuit model for a two-port disk resonator. ..... 55

Figure 3.1 Cross-section view of a single wine-glass disk resonator on SOI substrate.... 56

Figure 3.2 Cross-section view process flow of a wine-glass disk resonator on SOI substrate. ..... 57

Figure 3.3 SEM, cross-section, and 3-D schematic view after the 1st lithography step and Si DRIE to define the resonator body structure. 58

Figure 3.4 SEM, cross-section and 3-D view after the 2nd lithography step and Si etch to define the electrodes. 59

Figure 3.5 SEM image, cross-section and 3-D view of the final device. 60

Figure 3.6 Schematic view of Bosch process principle. 61

Figure 3.7 Schematic view graph of the two-step Bosch process. 62

Figure 3.8 A simplified model for the Bosch process: in one deposition/etch cycle, the deposition step lasts for a period of $t_1$, and the etch step for $t_2$, which includes both polymer removal and Si isotropic etch. 63

Figure 3.9 SEM photos of DRIE Si sidewalls (a) before and (b) after oxygen plasma treatment. 64

Figure 3.10 Si etch time vs. (a) source power, (b) $SF_6$ pulse time, and (c) $C_4F_8/O_2$ pulse time. 65

Figure 3.11 SEM photos of Si sidewall scalloping formed by different Si DRIE recipes: (a) original recipe A; (b) recipe B with reduced source power; (c) recipe C with reduced $SF_6$ pulse time; (d) recipe D with increased $C_4F_8/O_2$ pulse time. 66

Figure 3.12 Overall Si etch rate decreases with increasing etch time. 67

Figure 3.13 Si etch rate decreases dramatically as aspect ratio increases. 68

Figure 3.14 Schematic concept of ALD process. 68

Figure 3.15 SEM image of a thin film of $HfO_2$ of ~ 50 nm deposited by ALD on Si substrate. 69

Figure 3.16 Etch rate in HF of $HfO_2$ deposited at different temperature and with different post-deposition treatment. 70

Figure 3.17 XRD spectra of ALD $HfO_2$ films on thermal oxide underlayer showing the effect of deposition temperature and annealing. 71

Figure 3.18 HF C-V measurement of a MOS capacitor with ALD $HfO_2$ film as dielectric. 72

Development of UHF Micromechanical Resonators and Arrays Based on Silicon-On-Insulator (SOI) Technology

Mingke Xiong

## ABSTRACT

A novel micromachining technology on SOI substrates is presented that is capable of producing on-chip high-$Q$ resonators and resonator arrays equipped with high aspect-ratio (30:1) microstructures and nano-gap capacitive transducers filled with high-k dielectrics. The newly developed IC-compatible MEMS microfabrication process consists of merely three standard photolithography steps, which is much simpler than the other SOI-based resonator device technologies. In order to achieve the optimum performance and yield of the resonators and resonator arrays, this SOI-based fabrication process has been carefully designed and investigated step by step.

For capacitively-transduced extensional mode (e.g., radial-contour and wine-glass mode) resonators, formation of nano-scale capacitive gaps and large resonator-to-electrode overlap area is essential for reducing the motional resistance $R_x$ and DC bias voltage by strengthening the capacitive transduction. Atomic Layer Deposition (ALD) technology with superb conformability and uniformity as well as outstanding thickness controllability is used to deposit the ultra-thin layer (~10 nm) of high-k dielectric material that acts as the solid capacitive gaps, which allows the mass production of on-chip capacitively-transduced resonators and resonator arrays with greatly enhanced

electromechancial coupling coefficient, and thus lower motional resistance and DC bias voltage.

Using this technique, high-$Q$ micromechanical resonators and resonator arrays on SOI substrates operating at ultra-high frequencies (UHF) have been developed. The ultimate goal of this project is to implement on-chip narrow-band micromechanical filters with unprecedented frequency selectivity and ultra-low insertion loss. By fine-tuning the nonlinear characteristics of the capacitive transducers enabled by the new SOI technology, novel on-chip mechanical signal processors for frequency manipulation, such as mixer and multiplier, will be investigated.

# CHAPTER 1 INTRODUCTION

Ever since David E. Hughes introduced the concept of electromagnetic waves in a signal system eight years before Hertz's experiments, wireless communication has gradually become one of the most exciting areas and has started to play an increasingly significant role in our everyday lives. Today, wireless communication technology makes impact on our lives in all aspects, such as cellular telegraphy, satellite communication, broadcasting, wireless sensor network, and a lot more [1]. Particularly, these achievements have led to a low-cost, power-efficient wireless communication system as well as the overwhelming boost of personal wireless communication devices like cellular phone, Global Positioning System (GPS), Personal Digital Assistant (PDA), portable PC, so on so forth. According to statistics released by Global System for Mobil Communications (GSM), the number of global GSM subscribers has surpassed 3 billion in 2008 and will continue to grow by over 10% annually.

However, the overly crowded spectrum, which is fully occupied by a wide variety of wireless communication standards, has imposed a big challenge in reception of the desired signal among substantial amount of interferences in adjacent frequencies. Hence, on-chip and fully integrated devices with better band selection are needed in order to catch up with the fast development of wireless communication system.

In order to satisfy the stringent specifications for communication standards, especially those based on traditional superheterodyne architecture, a number of high quality ($Q$)-factor mechanical components are required for precise frequency generation

and selection. So far, tremendous efforts have been devoted to using alternative transceiver architectures, such as direct conversion (zero-IF) [2], low-IF [3, 4], and RF sampling down-conversion [5], which rely on higher levels of transistor integration to minimize the need for high-$Q$ passives at RF front-ends. Unfortunately, performances of them are not ready yet to compete with that of their counterparts in traditional superheterodyne architecture, thus trumpeting a need for on-chip replacements of the high-$Q$ RF passives (e.g., filters, resonators, etc.).

Recent development in the radio frequency micro-electro-mechanical systems (RF MEMS) technology has attracted a great deal of attention from both academia and industries, which holds great promises to potentially revolutionize the entire regime of the wireless technology by bringing together microelectronics and micromechanical elements. As such, the implementation of complete wireless transceivers on a single chip could lead to a viable solution to many current issues and challenges in present-day wireless communications. Particularly, due to their orders-of-magnitude smaller size as compared to traditional off-chip passives (e.g., quartz crystal, ceramics, etc.), the next generation of wireless transceivers equipped with RF MEMS components can be realized with greatly enhanced performance. A CMOS-compatible MEMS technology has been demonstrated lately that enables alternative communication architecture by facilitating the integration of high-$Q$ passive devices with active transistor electronics, allowing great size reduction, lower power consumption and enhanced performance [6].

Among the various types of MEMS devices and applications, capacitively-transduced micromechanical resonators have obtained most interests due to their UHF to SHF operation frequencies and ultra-high $Q$-factors exceeding 10,000 [7-11]. In addition

to their superb frequency selectivity, the use of capacitive transduction makes the resonators operating under electric charge potentials with no dc current flow thus no dc power consumption. Moreover, due to the fact that the resonance frequency is defined by the lateral dimensions, capacitively-transduced resonator offers CAD layout-definable frequencies. Other benefits include better thermal stability [12], higher frequency stability [13], better voltage-controlled tunability [14], better CMOS-compatibility, and self-switching capability [15].

### 1.1 Background of Wireless Transceiver Architecture

A transceiver is a device that consists of both a transmitter and a receiver sharing the same electronic circuitry. A transmitter modulates the baseband data and up-converts it into a carrier frequency with sufficient power amplification. Key parameters of the transmitter performance are the modulation accuracy, signal purity, and RF output power level. The main function of a receiver is to demodulate the desired signal from the presence of undesired interference and noise. Therefore, comparing to a transmitter which processes a locally available strong signal, a receiver is much more challenging because of the requirement of high dynamic range and high out-of-band attenuation.

Due to the increasing data traffic, the associated signal bandwidth is limited. As a result, selectivity becomes the most important characteristic of a receiver, which is defined by the capability of picking up the wanted signal while rejecting adjacent frequency interferers. Filters with high off-band attenuation are used to select the narrow band channels. The selectivity of a filter is determined by its quality factor, $Q$, given by:

$$Q = \frac{f_0}{BW} \tag{1.1}$$

where $f_0$ is the center frequency and $BW$ the 3 dB bandwidth of the filter.

In the following sections, several most popular receiver architectures and a novel MEMS-based architecture proposed this work are discussed.

### 1.1.1 Superheterodyne Architecture

Since invented by Edwin Armstrong in 1917, superheterodyne architecture has still been used within a majority of wireless systems. As illustrated in Figure 1.1, the desired signal received by an antenna passes through a pre-select bandpass filter, a low noise amplifier (LNA), and then an image-reject filter to remove the out-of-band interference as well as the image frequency. The selected RF signal is then converted to an intermediate frequency (IF) signal by mixing with a local oscillator (LO) signal generated by a voltage controlled oscillator (VCO). A channel-select filter is used to assign the desired channel and reject all the in-band interference. This is followed by an analog-to-digital converter (ADC) and a digital signal processor (DSP) that perform the demodulation and data decoding to provide the output baseband data, respectively.

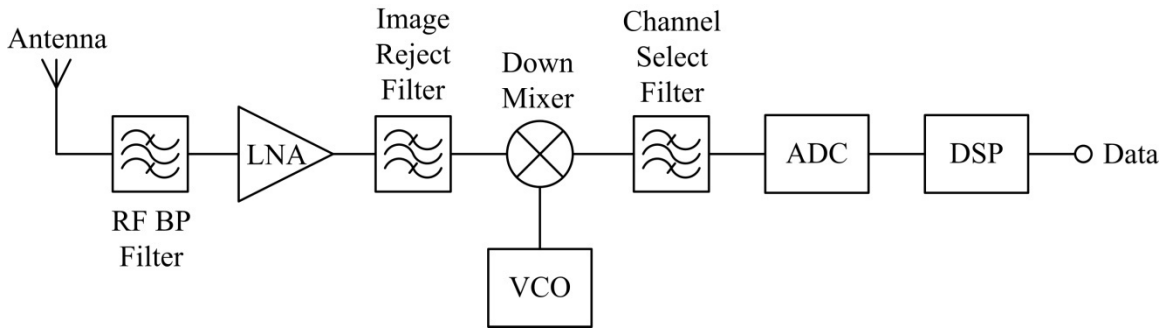


Figure 1.1 Simplified architecture of a superheterodyne receiver with single down-conversion.

As shown in Figure 1.1, high-$Q$ vibrating mechanical components, such as ceramics, quartz crystal, and surface acoustic wave (SAW) resonator are used to integrate with bandpass filters and oscillators. Filters utilizing such technologies successfully

extinguish themselves by outstanding quality factor, low insertion loss, high percent bandwidth, and high out-of-band rejection [16]. Oscillators also benefit from high-$Q$ because the phase noise decreases as $Q$ increases. However, as the demand for high-selectivity devices keeps on increasing, quartz and SAW devices have gradually failed to satisfy the stringent high-$Q$ requirement. More importantly, current high-$Q$ devices are bulky, where off-chip components make the ultimate miniaturization of the wireless communication systems difficult.

### 1.1.2 Direct Conversion Architecture

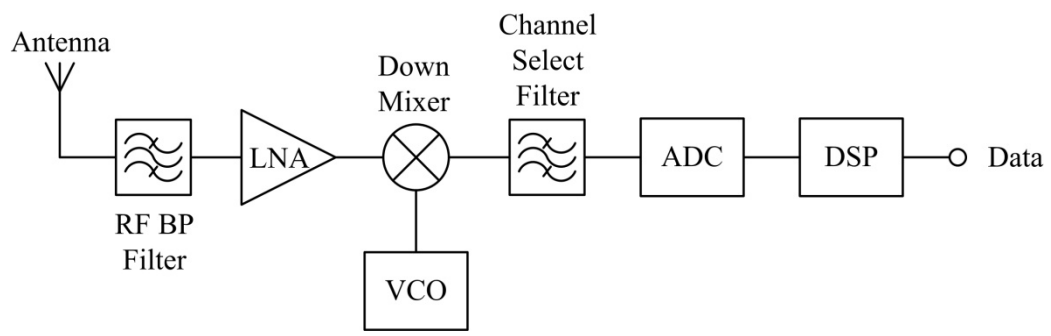


Figure 1.2 Simplified architecture of direct conversion receiver.

The motivation of ever increasing integration level has led to the invention of the direct conversion receiver, which is also known as "homodyne" or "zero-IF" [3, 4]. Figure 1.2 shows a simplified architecture of direct conversion receiver. As the local oscillator frequency in direct conversion receiver is set equal to the RF frequency, the IF frequency becomes zero and the image frequency could be successfully eliminated. Hence, eliminating image-reject filter that is required in superheterodyne architecture enables the reduction of the number of off-chip components. Nevertheless, several issues remain in today's communication system. The LO-leakage due to the settings of the same RF and LO frequency results in a time-varying dc offset, and can lead to degradation of

the upper boundary of the dynamic range. Thus, complicated offset cancellation techniques are needed in practical implementations.

### 1.1.3 Architecture Based on RF MEMS Resonator

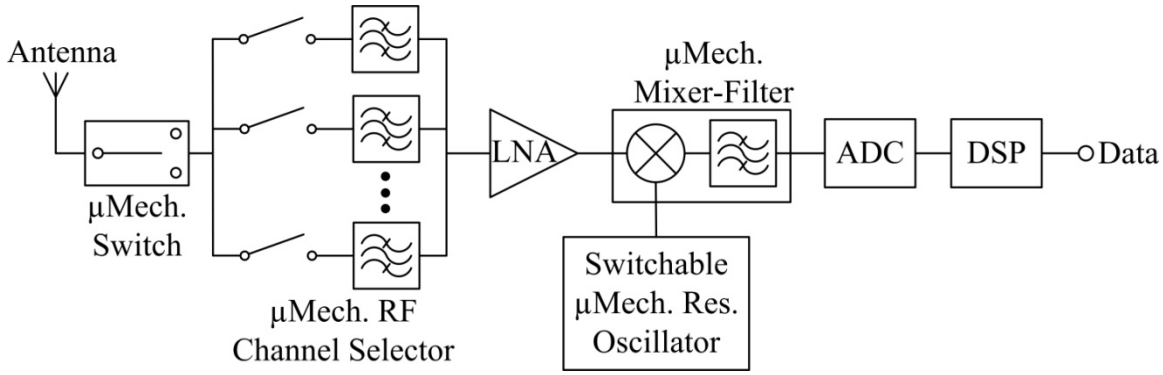


Figure 1.3 Simplified architecture of RF MEMS resonator-based channel select receiver.

Considering the size and extra cost of the large quantity discrete high-*Q* components, a technology that can realize the multi-channel selection on a single chip monolithic implementation will be highly desirable. Recent advances of CMOS-compatible micro-electro-mechanical-system (MEMS) technology has made it possible to implement on-chip RF MEMS elements, which are able to not only reduce the size, cost and power consumption, but also achieve better performances (high frequency, high-*Q*, high dynamic range, sharp cut-off, etc.). Aside from direct replacement of the off-chip high-*Q* passive devices, an RF channel-select architecture has been demonstrated [6]. Figure 1.3 presents the system block diagram for a newly-invented RF channel select receiver that takes full advantages of achievable complexity utilizing MEMS elements. CMOS-compatible micromechanical devices with high-*Q* (>10,000) and high frequencies (>1 GHz) have been reported recently [7-10, 17, 18], providing the potential of integration of wireless communication system. In addition to miniaturization, if channel selection is possible at RF carrier frequencies, succeeding electronic components such as

LNA and mixer are no longer needed to handle the power of alternate channel interference. Therefore, dynamic range can be greatly relaxed, allowing significant reduction in power consumption as well as the cost.

## 1.2 Macro-scale Vibrating Mechanical Resonator for Wireless Communication

Nowadays, frequency-selective mechanical components, such as ceramic and quartz crystal resonators, are needed for RF and IF bandpass filtering and local oscillator reference frequency generation. Outstanding performances have been achieved including low insertion loss, small percent bandwidth, sharp cut-off, and dynamic range. However, the most popular RF passives are all off-chip components that must interface with transistor at the board level, thus imposing two main technical challenges in next-generation multiband wireless transceivers: size and cost. The following sections will focus on the status of current off-chip components used in wireless communications and then explain the requirement for their replacement.

### 1.2.1 Ceramic Device

Piezoelectric materials, such as barium titanate and Lead-Zirconate-Titanate (PZT), have been used in many fields since the discovery of piezoelectric effect in 1880. Barium titanate ceramic is a good candidate for electromechanical transducers because of their high electromechanical coupling coefficient, ease of fabrication, and non water solubility. However, two key weakness of this material have greatly limited its further development, namely bad temperature coefficient and low Curie point. On the other since PZT ceramics are discovered in 1954, they have rapidly taken the places of barium titanate in most piezoelectric applications due to their high electromechanical coupling factor, good frequency-temperature characteristics, and suitable quality factor.

Various types of ceramics with high dielectric constant and good temperature stability have been investigated and implemented into practical dielectric filters over the past decades [19-22]. The dielectric filters at frequencies up to 75 GHz have been widely used in wireless communication applications. However, ceramic filters have been facing the issue of "bulky" size as the increasing requirement of miniaturization of wireless communication systems.

### 1.2.2 Quartz Crystal Device

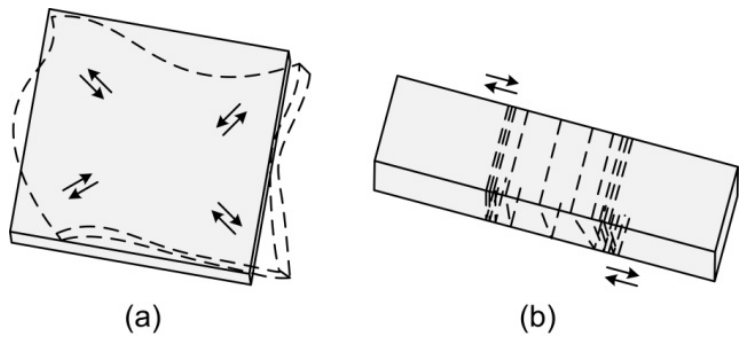


Figure 1.4 Mode shapes of quartz crystal unit: (a) contour shear mode; (b) thickness shear mode.

Quartz crystal is made of single crystal silica that has piezoelectric properties. Quartz crystal has various vibration modes according to its crystallinity and piezoelectricity. Parameters that determine the resonance frequency are different depending on the vibration mode. As shown in Figure 1.4 frequencies of a contour shear mode resonator (CT cut, DT cut) and a thickness shear mode resonator (AT cut, BT cut) are determined by the length of one side of the square and the thickness, respectively. Some of the vibration modes, such as AT cut and GT cut crystal units, have zero temperature coefficient over a broad temperature range, and therefore these two crystal units have excellent frequency-temperature characteristics. Moreover, quartz crystal is extremely stable both physically and chemically – no significant frequency change after

aging, which permits the widely use of quartz crystals with accurate frequency control [23], timing[24, 25] and filtration [26, 27].

In particular, among the off-chip components in wireless communication transducers, quartz crystal used in reference oscillators is the most difficult to be miniaturized and integrated on chip, since the its *Q*-factor is too high to be matched by current on-chip devices. The *Q*'s of on-chip elements such as on-chip spiral inductor for the LC tank, on conventional CMOS silicon are limited to less than 10, nowhere near the required high quality factor for reference oscillators [28]. Hence, lots of efforts are focused on finding replacements for the high-*Q* but bulky quartz crystals that dominate the market of reference oscillators. An ultrahigh-*Q* oscillator based on 60 MHz wine-glass mode disk resonator using a hybrid combination of on-chip components (see section 1.3.2.3 ), has exhibited an oscillator phase noise of -110 dBc/Hz at 1-kHz offset from the carrier, and -132 dBc/Hz at far-from-carrier offsets. Astonishing performances make this technique a very promising alternative to quartz crystal to meet the GSM reference oscillator phase noise performance specifications (of -130 dBc/Hz at 1-kHz offset from a 13-MHz carrier and -150 dBc/Hz at far-from-carrier offsets).

### 1.3 Micromechanical Resonators for Wireless Communication

Due to the ever increasing demand for multi-band and multi-functional wireless handsets, on-chip high-*Q* resonators have become the only viable choice for numerous future wireless applications. Although nanomechanical resonators have been proven with their ability to operate at GHz frequencies even in their fundamental mode [29, 30], they are also more susceptible to scaling-induced performance limitations, such as the adsorption/desorption noise and temperature fluctuation noise, than their MEMS

counterparts. For instance, noise sources such as Brownian motion and Johnson noise, which are considered negligible for most of MEMS devices, become significant as the sizes of nanomechanical resonators continue to shrink [31]. Additionally, insufficient power handling is another issue that may hinder the rapid deployment of NEMS devices in wireless systems to satisfy today's communication standards. Even though packaging devices under proper pressure and temperature conditions may mitigate the noise problems, the more serious constraints in power handling ability would remain unresolved. Moreover, both MEMS and NEMS resonators operate with higher motional impedance than their macro-scale counterparts. Hence, in order to seamlessly interface the MEMS/NEMS resonators with the macro-scale electronics such as antennas, strategies for reducing their equivalent motional impedance are urgently needed. This paper will review both device-level and system-level methodologies for lowering the motional impedance of the resonators. As such, the implementation of capacitive transducers filled with high-k dielectrics to improve the electromechanical coupling coefficient would be considered as one of the device-level methods; whereas parallel combination of a large array of resonators enables reduction of the motional impedance while improving the overall linearity and power handling ability would be treated as a system-level approach. In terms of the readiness to be inserted into 50 Ω-matched wireless subsystems, MEMS resonators would be a much more practical choice comparing to NEMS. Therefore, development of MEMS resonators becomes essential for realization of the next-generation wireless systems.

### 1.3.1 Piezoelectrically-Actuated Resonators

Piezoelectric materials, such as zinc oxide, aluminum nitride, barium titanate and lead-zirconate-titanate (PZT), have been widely studied for numerous device applications since its discovery in 1880. Piezoelectric material deforms when an electric field is applied, whereas any strain induced in piezoelectric material generates charges within the material. A simple piezoelectrically-actuated resonator consists of a piezoelectric material and a mechanical structure along with strategically placed electrodes, which are employed to facilitate the coupling between the mechanical and electrical domains. When the applied ac signal matches the resonance frequency with a particular mode shape of interest, the MEMS resonator will vibrate at its resonance. Different types of piezoelectrically-actuated resonators are discussed and compared in this section.

#### 1.3.1.1 Surface Acoustic Wave (SAW) Resonators

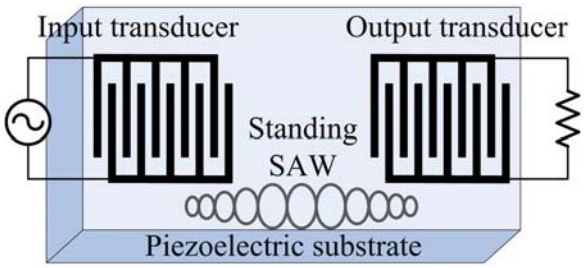


Figure 1.5 Schematic of a typical SAW resonator [32].

A Surface Acoustic Wave (SAW) resonator consists of three parts, as illustrated in Figure 1.5: piezoelectric substrate, interdigital finger transducers (IDT) locating on the crystal surface, and reflectors disposed near the opposite ends of IDT. The SAW resonator utilize surface acoustic wave vibrating between two reflectors and the resonant frequency is determined by both the width of IDT and spacing between two fingers. The equation can be expressed as

$$f = \frac{v_s}{\lambda} \quad 1.2$$

where $v_s$ is the velocity of the surface acoustic wave in the piezoelectric substrate, and $\lambda$ is the pattern period of the IDT, as shown in Figure 1.5.

Unlike the bulk-acoustic-wave device, acoustic energy propagates along and is confined to a single surface of the substrate. Hence, SAW devices are not as sensitive as their bulk-acoustic-wave counterparts to the substrate shape or scale, resulting in a much easier design and fabrication. In addition, due to the lower power density that occurs in the distributed geometry, SAW devices have superior power handling capability as compared to bulk-wave devices. As a result of these advantages, SAW devices are widely used in today's wireless communication systems [33].

#### 1.3.1.2 Bulk Acoustic Wave (BAW) Resonators

Another type of acoustic wave is bulk acoustic wave (BAW). Unlike surface acoustic wave, the bulk acoustic wave travels from one surface through the bulk material to the other surface to form so called bulk acoustic wave. BAW devices usually operate with resonance frequencies of 1~20 GHz [34-37]. BAW resonators have many features superior to mostly used devices such as SAW devices and ceramic devices. Comparing to ceramic and SAW devices, it has a high $Q$-factor that leads to low insertion loss and sharp cut-off characteristics and low power consumption with reduced size. Figure 1.6 shows the Agilent process using free-standing membranes that are anchored at edges to the silicon substrate.

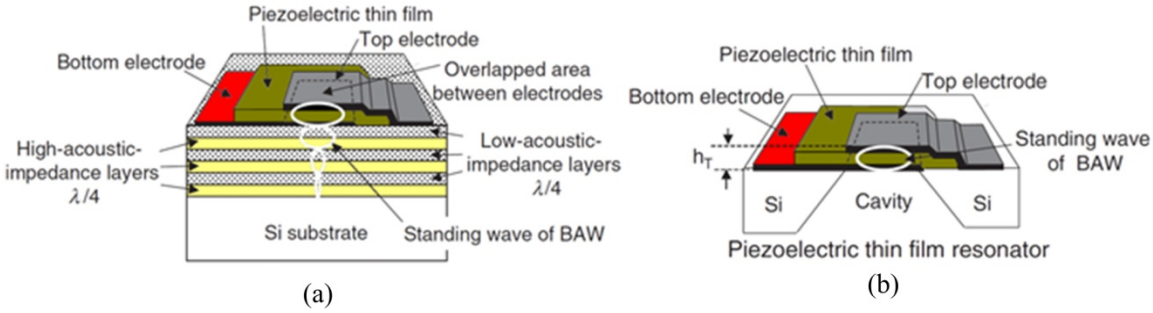


Figure 1.6 Device implementation for the two types of bulk acoustic wave (BAW) resonators with two different types of acoustic isolation methods [32]: (a) SMR employs Bragg's reflector; and (b) FBAR sits on top of air cavity.

In a typical BAW device, the acoustic layer is stacked in between the top and bottom electrodes, where the acoustic wave is confined. The performance of a BAW device is heavily dependent upon the impedance mismatch on the boundary of the piezoelectric body which helps trapping the as-generated acoustic wave within. Two different kinds of implementation are mostly used, as illustrated in Figure 1.6: solid mounted resonator (SMR) and film bulk acoustic resonator (FBAR). In SMR, the BAW structure is sitting on top of multiple reflective layers (Bragg's reflector) [38] to reflect/retain the acoustic wave back into the piezoelectric film. On the other hand, FBAR simply uses an air cavity to create a huge impedance mismatch. The operation principles of SMR and FBAR are the same except the technology employed to provide the acoustic isolation. Compared to SMR, FBAR is much easier to fabricate as it does not require the perfect quarter wave length reflective layers. Since 2002, FBAR has been widely employed for wireless telecommunications.

However, in order to achieve precise frequencies and a better yield, the thickness of each thin film must be accurately controlled from device to device, which may cause a serious problem in FBAR device fabrication. Nevertheless, as wireless communication

technology pushing towards to the ultimate miniaturization, multi-function transceivers that operate at different frequencies instead of a set of several discrete components are soon going to be needed, which is a serious bottleneck against the current FBAR technology.

Recently, due to the advance of micromachining technology, a new type of BAR device has attracted large attention. Unlike conventional FBARs, the novel contour-mode FBAR device (see Figure 1.7) uses its lateral dimension (i.e., radius of the disk or the width of the ring) to control resonance frequency, thus allowing implementation of multiple frequency circuitries on a single chip. It has been proven that piezoelectrically-transduced contour-mode resonators have unique characteristics, such as a CAD-layout definable resonance frequency, high quality factor up to 4,300 at 230 MHz and low motional impedance (50~700 Ω), thus making it a perfect candidate as the key building block for the next generation wireless transceivers [39, 40].

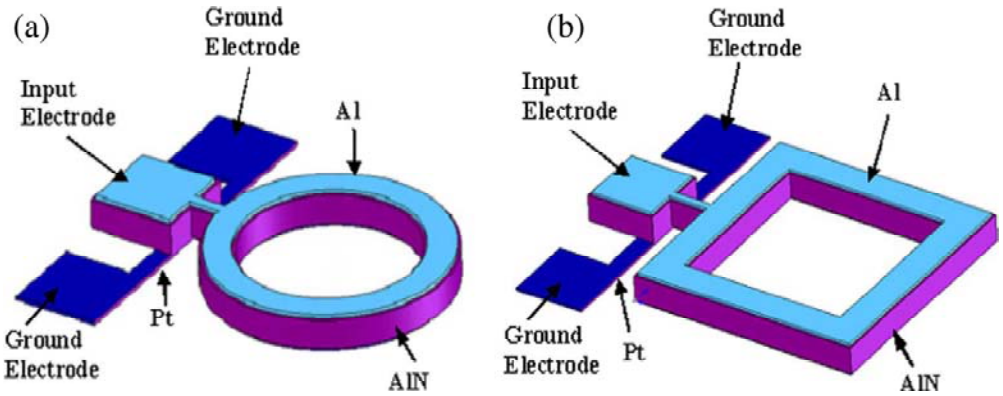


Figure 1.7 Contour mode ring resonator [39]: (a) one port circular ring resonator; (b) one port square-shape ring resonator.

Figure 1.8 depicts the top-view image and measured frequency characteristics of post-CMOS compatible AlN-based dual-mode filter developed by Sandia National Laboratory, which employs an unique molded tungsten (W) technique along with the

AlN process to realize potentially higher $Q$ [41]. In addition, this technology allows the scaling of AlN resonators into the GHz range without introducing spurious modes or reducing the quality factor, but offering acceptable power handling for both the transmit and receive paths in full-duplex radios.

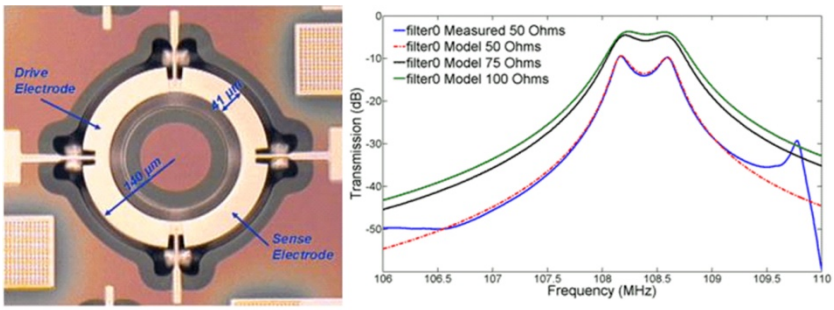


(a) (b)

Figure 1.8 (a) Photo of an AlN dual-mode filter; (b) measured transmission (S21) of the AlN dual-mode filter, along with simulated response based on its equivalent circuit model with different termination impedance [41].

As good as it seems to be, these newly-emerged piezoelectric MEMS resonators still have some remaining issues to be addressed. On one hand, the FBAR resonator, whose resonance frequency is controlled by its thickness, is not amenable to realization of multiple frequencies on a single-chip. On the other hand, piezoelectrically-transduced contour-mode resonators suffer from its relatively low frequencies. In addition, the relatively large temperature coefficient in the range of 25 ppm/°C [42] as opposed to 2 ppm/°C [43] of less for capacitively-transduced resonators is yet another concern. In order to overcome these issues, there are ongoing research studies which focus on optimization of piezoelectrically-transduced MEMS resonators.

### 1.3.2 Capacitively-Transduced MEMS Resonators

Capacitively-transduced resonator offers in general the highest frequency-$Q$ product among micromechanical resonators, due to the employment of high quality structural material which is much less susceptible to acoustic losses to the substrate as opposed to piezoelectrically-actuated resonators. Besides the high frequency selectivity, the use of capacitive transduction also allows the resonators to operate under a dc bias voltage without dc current flow, thus consuming ultra-low dc power. Moreover, capacitive transduction is also employed in large part to simplify future integration with transistors. Additionally, the employment of extensional-mode resonators with CAD-layout definable resonance frequencies provide a solution to resolve the key limitations of the conventional film bulk acoustic resonators (FBARs), in which the thickness of the piezoelectric film determines the resonance frequency. Unfortunately, the majority of capacitively-transduced MEMS resonators developed so far suffer from their excessive motional impedance, which hinders their direct implementation into the wireless systems. On the contrary, much lower motional impedance in the range of 50 Ω can be easily obtained in MEMS resonators equipped with piezoelectric transducers.

This section reviews recent progress in the research and development of MEMS resonators in silicon and CVD diamond materials for wireless communications, with a particular focus on existing and possible solutions of the aforementioned issues.

#### 1.3.2.1 Flexural Mode Beam Resonator

Vibrating beam micromechanical resonators have attained a great deal of attention over the past few years, due to their achievable VHF and UHF ranges, high $Q$'s, tiny sizes, and virtually zero dc power consumption. Three different types of beam resonators

have been widely investigated and utilized in various areas, including sensing, actuation and communication [43]. Categorized by their boundary conditions, they are clamped-free beam resonators (i.e., cantilevers) [44], clamped-clamped beam resonators [45, 46], and free-free beam resonators [47], shown by Figure 1.9 (a), (b), and (c), respectively.

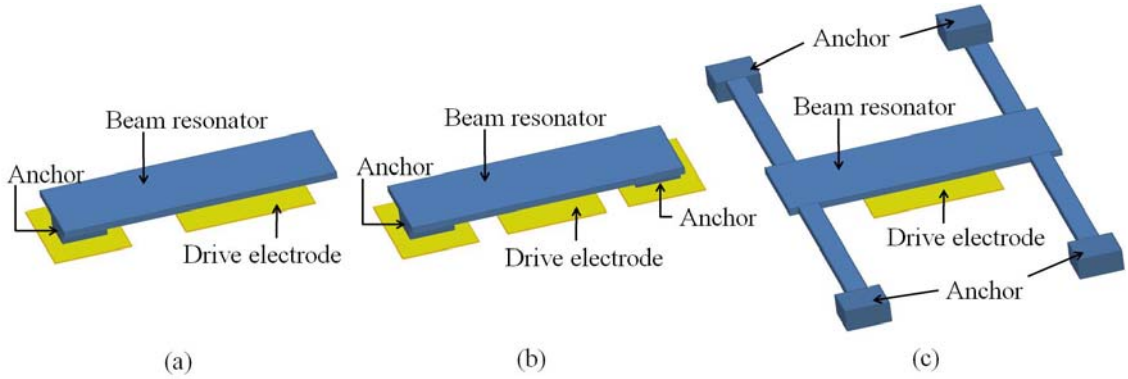


Figure 1.9 Schematic view of different types of beam resonators: (a) cantilever beam resonator; (b) clamped-clamped beam resonator; (c) free-free beam resonator.

Cantilevers have much lower resonant frequencies and worse dynamic range when compared to free-free beam and clamped-clamped beam resonators because of their relatively low stiffness. However, for the case of clamped-clamped beam resonators, larger stiffness is gained at the cost of higher anchor dissipation, which makes it much harder to achieve high-$Q$ at high frequencies - $Q$ reduces from 3,000 to less than 300 when resonant frequency increases from 10 MHz to 70 MHz. Although high $Q$-factor can be achieved by shrinking dimensions (masses) of clamped-clamped beam resonators [48], inadequate dynamic range and power handling capability of such devices are hard to satisfy most communication applications.

On the other hand, free-free beam resonator has been demonstrated with center frequency of 30 ~ 90 MHz and $Q$ of ~8000 [47]. As shown in Figure 1.9 (c), the free-free beam resonator is supported at its flexural node points by four torsional beams which are

anchored to the substrate. The supporting torsional beams are designed with quarter-wavelength dimensions, which acoustically isolate the free-free beam from the rigid anchors. Thus, ideally, the free-free beam operates as if it is levitated without any anchor. The ideally eliminated anchor dissipation enables the free-free beam design greatly surpasses previous clamped-clamped beam resonators, allowing much higher $Q$-factor.

#### 1.3.2.2 Radial-Contour Mode Disk Resonator

Polysilicon micromechanical radial-contour mode disk resonators have been firstly demonstrated with $Q$'s over 1500 at frequency of 1.14 GHz in vacuum and air, respectively [49]. One year later, the similar resonator with resonance frequency up to 1.156 GHz along with measured $Q$'s > 2650 has been reported. In addition, a 734.6-MHz version has been demonstrated with $Q$'s of 7,890 and 5,160 in vacuum and air, respectively [9]. Figure 1.10 shows the SEM picture and frequency response spectrum of a polysilicon self-aligned radial-contour mode disk resonator.

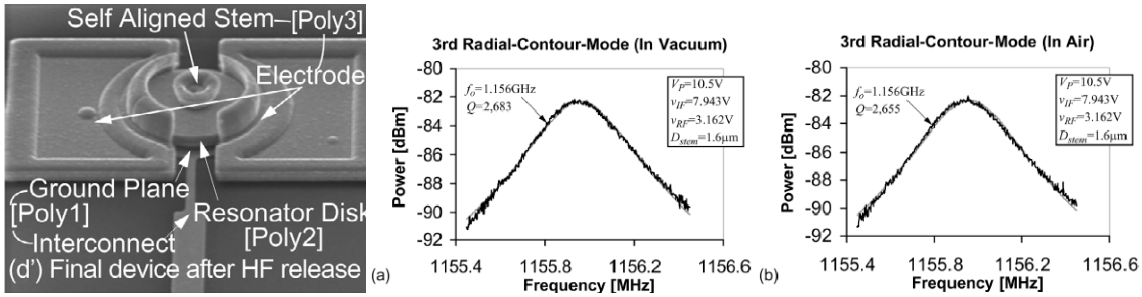


Figure 1.10 SEM image and measured frequency response in (a) vacuum and (b) air for a polysilicon capacitively-transduced radial-contour mode disk resonator [9].

Self-alignment of the supporting stem to the exact center of the resonator disk allowing the superior symmetrical modal vibration of the resonator is the key to obtain high-$Q$ at gigahertz frequency range while retaining the similar micro-scale dimensions and adequate power handling. Self-alignment allows the resonator disk being supported

by the stem at the motionless nodal point at the center of the disk during its pure radial vibration, and minimizes the energy loss to the substrate from the center anchor, thus allowing high-$Q$ in spite of the high resonator stiffness that is essential for maintaining decent power handling capability. As illustrated in Figure 1.11, the self-aligned center anchor is achieved by defining both the stem position and the disk edges during a single lithography step (i.e. in one mask), which effectively eliminate the misalignment between two different masks (the first one defines the stem and the second mask aligned to the previously patterned stem to pattern the disk around the center stem), as opposed to previous resonator designs [50]. Another difference between this self-aligned disk resonator and the previous one is that an electrically accessible substrate contact is included in the present design, which successfully eliminates feedthrough current and allows much cleaner measurement of frequency characteristics (see Figure 1.12).

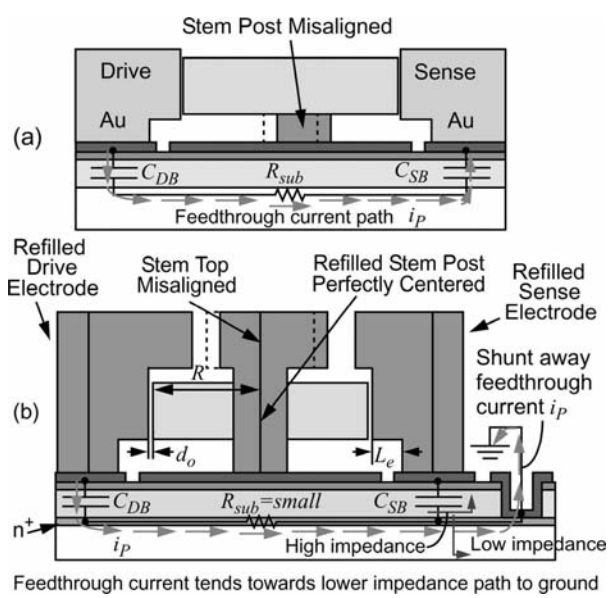


Figure 1.11 Comparison between (a) a previous disk resonator process; (b) the self-aligned disk resonator process [9].

The complete process flow of the self-aligned radial-contour mode disk resonator is illustrated in Figure 1.12: (a) a layer of high-temperature oxide (HTO) is deposited on $n^+$ Si substrate by LPCVD, followed by a layer of LPCVD $Si_3N_4$; (b) substrate contact trenches are dug through the $SiO_2/Si_3N_4$ layer by wet/dry etch, then the first layer of polysilicon is deposited via LPCVD and $POCl_3$ doped, and finally patterned to form ground planes, interconnects and substrate contact pads; (c) a field HTO is deposited via LPCVD, followed by the structural $POCl_3$ doped LPCVD polysilicon layer, and then capped with a film of HTO served as the hard mask for structural polysilicon dry etch and as the spacer layer to separate the disk and the overhanging electrodes; (d) after annealed in $N_2$ atmosphere for an hour, the spacer HTO film and the structural polysilicon layer are patterned, defining not only the shape of the disk but also an opening at the center of the disk, which is eventually the location of the stem; (e) an LPCVD sidewall sacrificial HTO layer is conformally deposited with a specific thickness that equals to the desired electrode-to-disk capacitive gap spacing; (f) the sidewall sacrificial HTO layer is removed in the stem opening, after which the stem and electrode via are opened down to the polysilicon substrate contacts; (g) a third layer of $POCl_3$ doped polysilicon is deposited and then patterned not only to define the side electrodes but also to refill the center via, forming a self-aligned stem; (f) the structure is released in HF to yield the final cross section view.

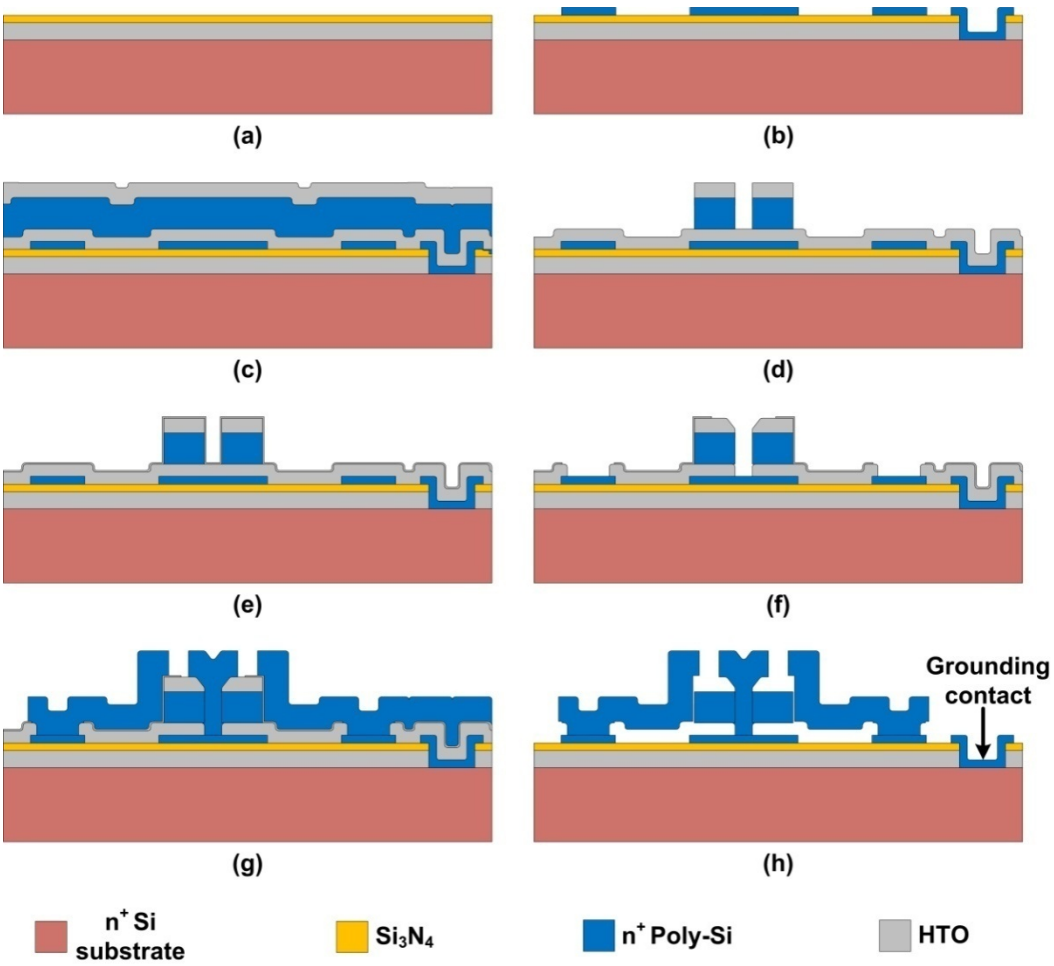


Figure 1.12 Fabrication process flow of the self-aligned radial-contour mode disk resonator.

#### 1.3.2.3 Wine-glass Disk Resonator

En route to pursuing higher-*Q*, polysilicon wine-glass mode disk resonator using a stem-less, side-supporting suspension structure has been demonstrated at frequency of 74 MHz with *Q*'s as high as 98,000 in vacuum and 8,600 in atmosphere [51] (see Figure 1.13). The lack of a center stem allows this device to minimize anchor losses, thus achieving higher *Q*. However, the device operates at a relatively lower frequency range due to the native of wine-glass vibration mode.

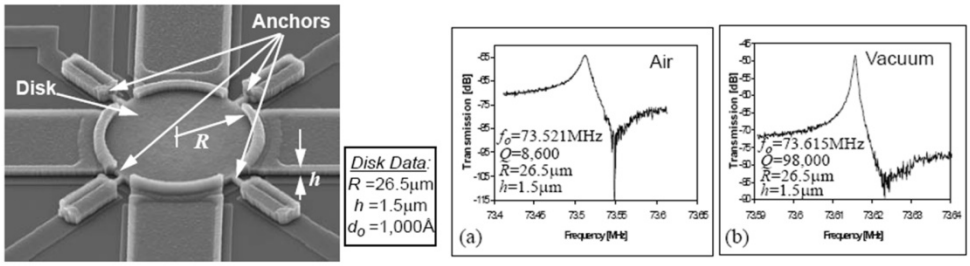


Figure 1.13 SEM photo and frequency response spectrum in (a) air and (b) vacuum of a polysilicon wine-glass mode disk resonator [51].

A perspective-view schematic of the wine-glass mode disk resonator in a typical two-port bias and excitation configuration is illustrated in Figure 1.14.

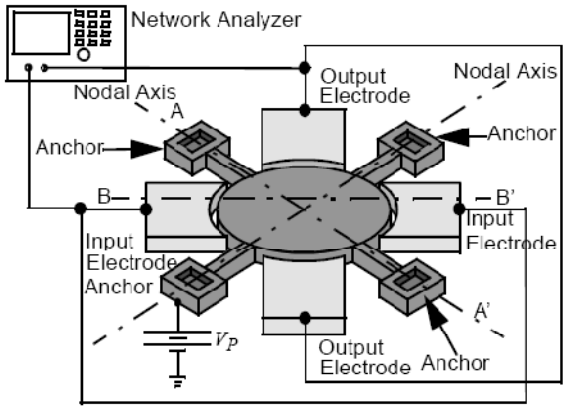


Figure 1.14 Perspective-view schematic of the wine-glass mode disk resonator in a typical two-port bias and excitation configuration.

### 1.3.2.4 Wine-glass Mode Ring Resonator

Despite the sufficient high-$Q$ and high frequency for applications of wireless communication achieved by the two aforementioned types of capacitively-transduced resonators (i.e. radial-contour mode disk resonator and wine-glass mode disk resonator), their large motional impedance (> 1 MΩ) is so far too high to compete with today's conventional RF components, which are designed to match to the front-end system impedance of 50 Ω.

An extensional wine-glass ring (EWGR) resonator structure [8], shown in Figure 1.15, has been designed so that the resonance frequency primarily depends upon the width of the ring other than the average radius, thus the ring's perimeter sidewall surface area is independent of its frequency. Because the motional impedance of a capactively-transduced resonator is proportional to the overlap area between the resonance structure and the electrodes, the impedance of the device can be strategically designed simply by choosing an appropriate radius without affecting its frequency. In order to achieve lower impedance than previous micromechanical resonators, inner and outer electrodes are used for a side-supported EWGR to increase the electrode-to-disk overlap area exhibiting a moderate impedance of 282 kΩ with DC-bias of 10 V at 1.2 GHz. In addition, the mode shape of the ring resonator combines the aspects of previously demonstrated modes, radial-contour mode [52] and wine-glass mode [51], to achieve the best of each design. Specifically, the EWGR structure allows ultra high resonance frequency due to the use of the radial-contour mode, and higher $Q$ because of stemless side-supporting structure resembling the wine-glass mode. As demonstrated in [8], frequencies as high as 1.2 GHz with a $Q$ of 3,700, and 1.52 GHz with a $Q$ of 2,800, have been successfully achieved, with the motional resistance 2.2 times lower than the measured resistance of the radial-contour mode disk counterparts.

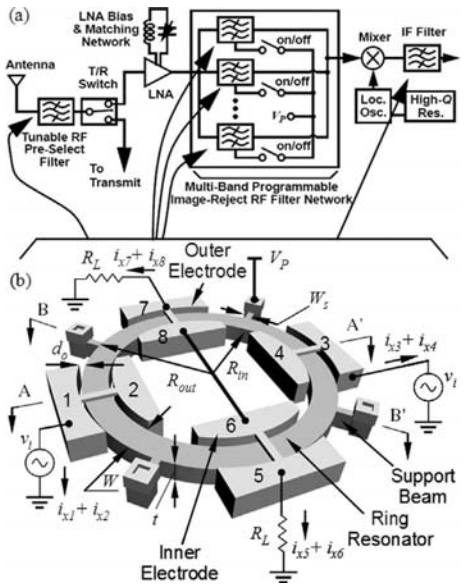


Figure 1.15 Perspective-view schematic of the extensional wine-glass ring (EWGR) resonator with typical driving and sensing configuration.

Moreover, by properly designing impedance-mismatched resonator-to-anchor transition, $Q$'s of 14,603 at 1.2 GHz has been achieved, as demonstrated by the spoke-supported "hollow disk" EWGR resonator [53]. The device is supported by a center stem with four supporting beams attached to the ring at notched nodal locations, achieving minimal anchor losses, thus raising $Q$ to 14,603 from 5,846 at 1.2 GHz. In addition, the supporting beams are designed to match the quarter wavelength of the resonance frequency to further prohibit energy dissipation from the center anchor to the resonance ring. SEM picture and measured frequency characteristics are shown in Figure 1.16 for the "hollow disk" EWGR device.

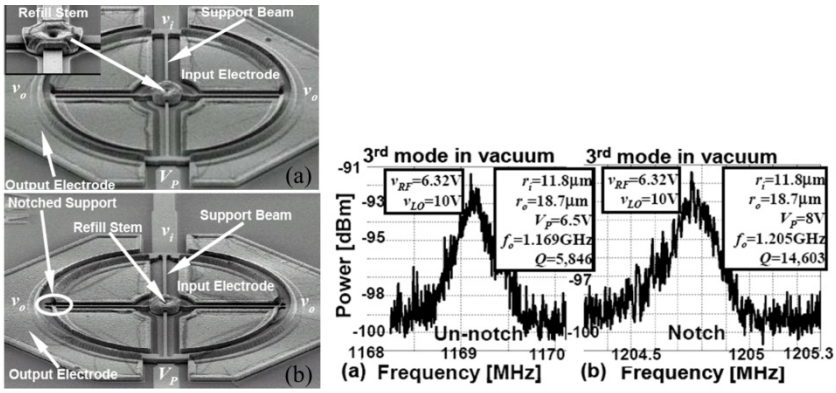


Figure 1.16 SEM picture and measured frequency characteristics of a (a) un-notched and (b) notched "hollow disk" EWGR device [53].

### 1.3.2.5 Internal Dielectrically-Transduced Bar Resonator

However, the cost of extending frequencies by scaling dimensions of MEMS resonators is greatly increased motional impedance $R_x$, which is a function of electrode-to-disk gap spacing, $d$, overlap area, $A$, and dielectric constant of the material using for the capacitive gap, $\varepsilon$, respectively, written as:

$$R_x = \frac{k_r}{\omega_0 Q V_P^2} \cdot \left(\frac{\partial C}{\partial x}\right)^{-2} \cong \frac{k_r}{\omega_0 Q V_P^2} \cdot \frac{d_0^4}{\varepsilon_r^2 \varepsilon_0^2 A^2} \qquad 1.3$$

Thereby, replacing air-gap that is employed by most capacitively-transduced resonators with solid gap filled by high-k dielectrics has several benefits. It is desirable to achieve smaller gap spacing, to prevent stiction symptoms of air-gap transducers, and to enhance capacitive sensing and reduce motional impedance due to higher dielectric constant, which will become even prominent as frequency goes higher and as the dielectric thickness approaches acoustic half-wave length in silicon [10]. A dielectrically-transducer silicon bar resonator with 15 nm nitride solid gap has been demonstrated with the so far highest resonance frequency of 6.2 GHz and $Q$ of 4,277 as shown in Figure 1.17. A frequency-$Q$ product of $3.1\times10^{13}$ at 4.7 GHz was also reported as the highest in

polysilicon reported to date [10]. A silicon bar resonator employing 10 nm air + 90 nm $HfO_2$ and 100 nm air capacitive gap exhibited an impedance of 1,256 Ω and 40,356 Ω, respectively, with $Q$ > 66,000 at 223 MHz, showing that high-k dielectric solid gap can effectively reduce the motional impedance [54].

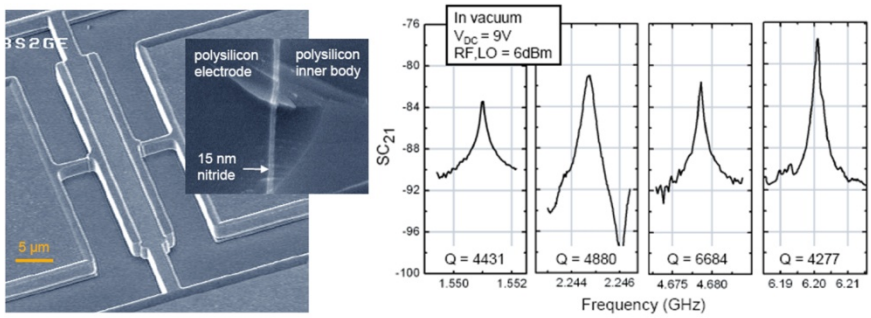


Figure 1.17 Picture of a bulk-mode resonator and the measured frequency characteristics at different vibrating mode [10].

### 1.3.3 Resonator Based on Silicon-on-Insulator (SOI) Technology

A lot of efforts have been made on VHF and UHF micromechanical resonators using polycrystalline silicon as the structural material. As demonstrated in the previous sections, astonishing performance of the resonators (i.e., high-$Q$, high frequency, etc.) have been achieved, however, higher-than-normal motional impedance is still the main issue that hinders its further development. Silicon-on-insulator (SOI) technology based on wafer bonding technique provides the possibility of greatly increased overlap area between resonator body and electrodes, which is able to reduce the motional impedance of the resonator while improving the power handling ability. Motional resistance as low as 43.3 kΩ has been measured for a 18 μm-thick disk resonator operating in its wine-glass mode at 149.3 MHz with $Q$ of 45,700 in vacuum and 25,900 in atmosphere, which is orders of magnitude smaller than the 883 kΩ of a 3 μm thick device [55].

In addition, comparing to conventional silicon substrate and surface micromachining, SOI technology distinguishes itself in several aspects: (1) the use of single crystal silicon as the structural layer other than commonly used polycrystalline silicon provides superior mechanical properties, such as lower energy dissipation due to less crystallographic defects [56] and lower internal stress [57]; (2) specific thickness, dopant type and concentration of the device silicon layer are available in commercial manufacturers, thus minimizing the need of the structural polysilicon deposition and doping during the fabrication process, which requires precisely controlled equipment and processing environment; (3) buried oxide layer offers superior dielectric isolation which protects the device Si layer from parasitic effects induced by the substrate [58].

Various techniques have been developed to fabricate suspended single Si structures on SOI substrate, which will be discussed and compared with each other in the following section, with a focus on the aspect of the fabrication techniques.

#### 1.3.3.1 Fabrication on SOI Substrate Utilizing Electron Beam Lithography

Electron beam lithography has been used for nanostructure patterning for years with resolution limit as low as several nm [59]. Combination of electron beam lithography and conventional silicon micromachining technique provides the possibility of fabricating MEMS devices with nano-scale structures.

A typical e-beam lithography-enabled MEMS device process includes four steps [60] as illustrated in Figure 1.18: (1) resist (e.g., PMMA) patterning by e-beam lithography; (2) metal lift-off; (3) Si anisotropic etching using metal as the hard mask; (4) underlying $SiO_2$ isotropic etching to suspended resonator's body.

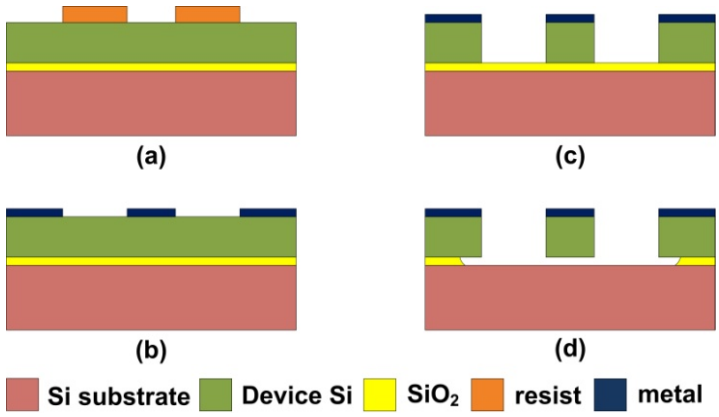


Figure 1.18 Fabrication process using e-beam lithography for creating suspended NEMS device on SOI substrate.

### 1.3.3.2 Fabrication on SOI Substrate Utilizing Focus Ion Beam (FIB) Technique

Focus Ion Beam (FIB), which uses $Ga^+$ ion to scan over the surface of a sample in a similar way as the electron beam in a scanning electron microscope (SEM), can mill a very narrow trench on Si substrate by accurately positioning on the sample at high current density [61], offering a promising alternative of conventional UV lithography technology to fabricate nano-scale electrode-to-disk gaps in a capacitively-transduced resonator. MEMS resonators with capacitive gaps less than 100 nm on thin SOI substrate has been demonstrated [62]. The fabrication process (see Figure 1.19) is based on a combination of standard UV lithography and a subsequent FIB milling with only two levels of photolithography, yielding the final SEM view in Figure 1.20.

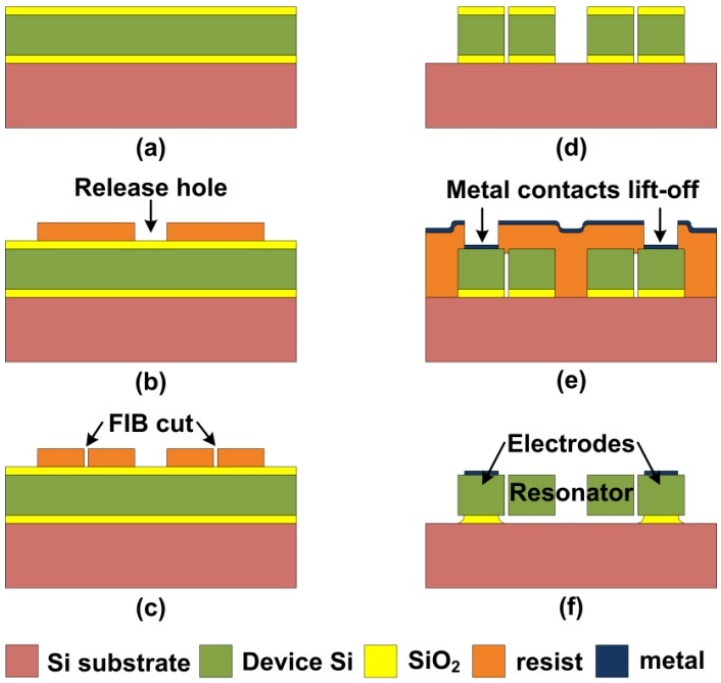


Figure 1.19 Schematic of the process of MEMS resonator with nano-gap utilizing FIB milling technique: (a) thermal oxide is grown on SOI wafer; (b) photolithography is used to open the release hole; (c) nano-scale gaps are achieved by FIB milling; (d) patterns are transferred to $SiO_2$/Si/$SiO_2$ layers by high aspect-ratio dry etch; (e) metal contacts are patterned by lift-off process after striping the top $SiO_2$ layer; (f) the resonators are released by etching away the buried oxide.

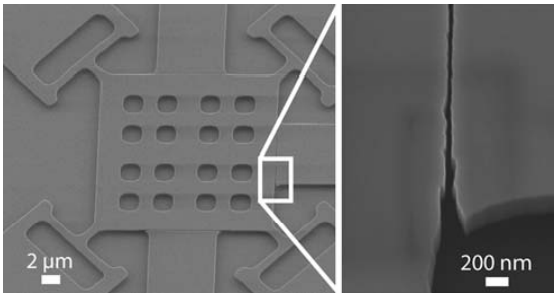


Figure 1.20 Bulk lateral resonator with narrow air gap (<100 nm) fabricated by the proposed FIB-based process [62].

#### 1.3.3.3 SOI Fabrication by Conventional Si Micromachining Technique

Although nano-scale devices and narrow capacitive gaps can be achieved by e-beam lithography and FIB technique, low productivity and high cost have hindered the further employment in mass production of micromechanical resonator fabrication. On the contrary, the conventional Si surface and bulk micromachining technique remains as the best choice to fabricate VHF/UHF and high-$Q$ capacitively-transduced resonators.

Single crystal silicon capacitively-transduced micromechanical resonators with sub-100 nm electrode-to-disk gaps based on high aspect-ratio poly and single crystal silicon (HARPSS) fabrication technique have been successfully demonstrated at VHF range with $Q$ as high as 45,700 in vacuum (see Figure 1.21) and 25,900 in atmosphere. Motional resistance as low as 43.3 kΩ has been measured for a 18 μm-thick disk resonator operating in its wine-glass mode at 149.3 MHz, which is orders of magnitude smaller than the 883 kΩ of a 3 μm thick device [55, 63, 64].

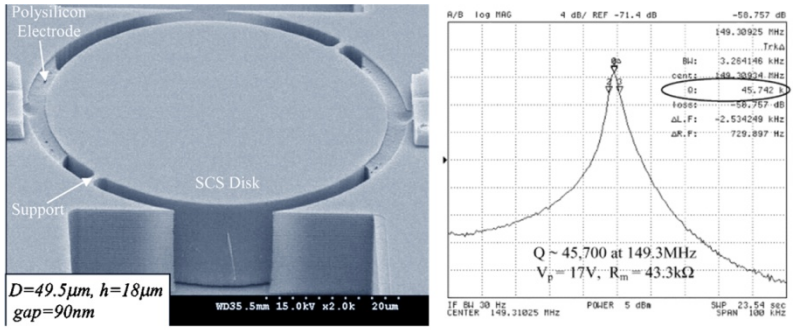


(a) (b)

Figure 1.21 (a) SEM image and (b) frequency response of an 18 μm-thick wine-glass disk resonator on SOI substrate [55].

The HARPSS fabrication process is shown in Figure 1.22: (a) thermal oxide is grown on SOI wafer and patterned, then $Si_3N_4$ is deposited by LPCVD and patterned by lithography; (b) trenches on device Si layer is etched by DRIE with $SiO_2/Si_3N_4$ as the

hard mask; (c) a thin layer of sacrificial oxide is deposited by HTO and is blanket etched on the surface, leaving only on the resonator sidewalls; (d) doped polysilicon is deposited by LPCVD and patterned on the surface to form the wire-bonding pads, then a thin layer of metal is deposited on the wire-bonding pads by e-beam evaporator; (e) releasing openings are etched in the device Si layer and the polysilicon inside trenches using photoresist mask; (f) buried oxide layer is removed by $SiO_2$ wet etch to suspend the device.

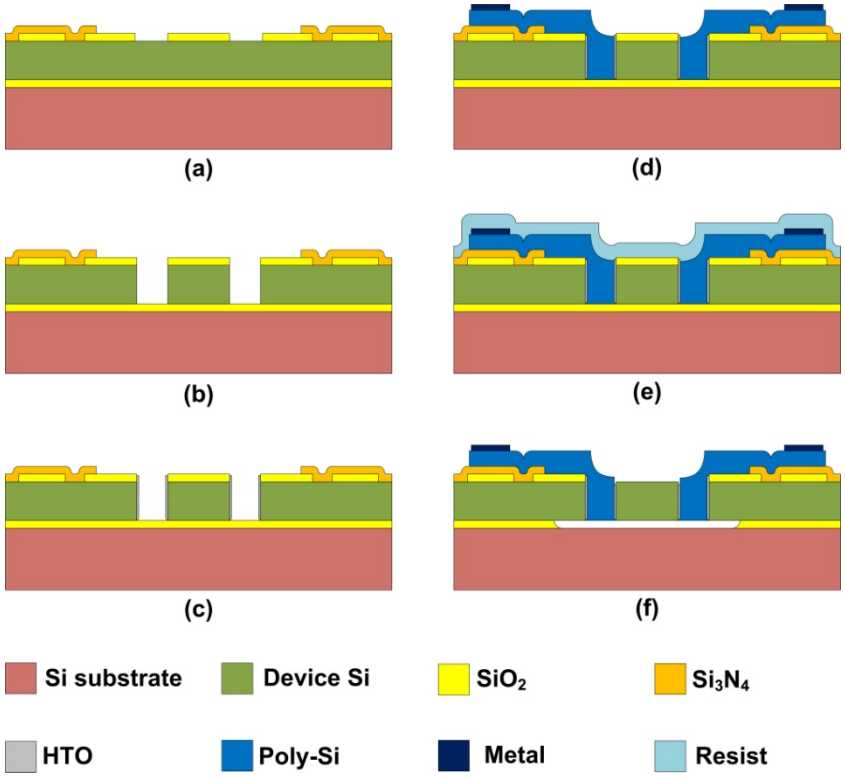


Figure 1.22 Fabrication process flow of HARPSS resonator on SOI substrates.

However as described above, the HARPSS process on SOI substrate consists of 6 lithography steps as well as several etching and deposition steps, which makes the fabrication process very complicated and time-consuming. A much simpler IC-compatible process on SOI substrate has been reported utilizing Chemical Mechanical Polishing (CMP), achieving 100 – 200 nm capacitive gaps with expected operating

frequency of the high-$Q$ resonator extend to MHz and GHz range [65]. Utilizing a similar fabrication process, study done by D. Grogg [66] has demonstrated a laterally vibrating bulk-mode resonators based on connected parallel beam resonators (PBRs) with $Q$ of 100,000 and motional impedance of 55 kΩ at 24.58 MHz.

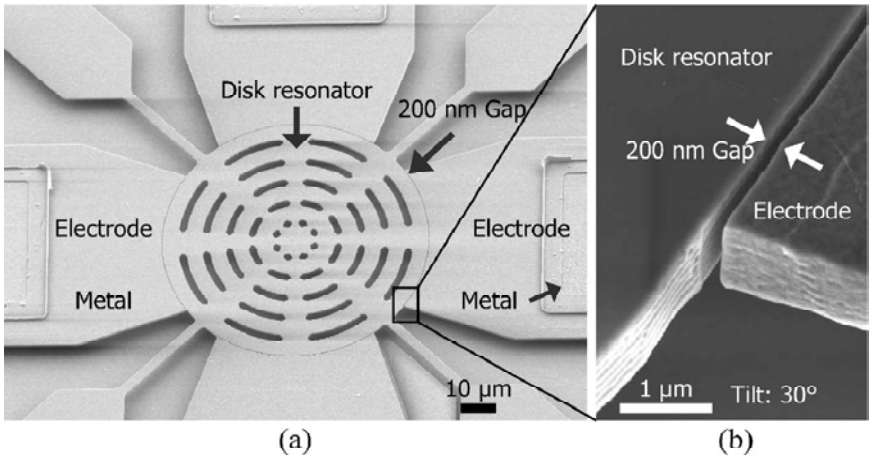


Figure 1.23 SEM image of (a) the disk resonator and (b) a zoom-in on the 200 nm gap [66].

The cross-section view of the CMP based fabrication process is illustrated in Figure 1.24: (a) starting with SOI substrate, a layer of LPCVD $SiO_2$ (TEOS) is deposited and then patterned, which defines the resonator disk structure, followed by a conformal coating of un-doped polysilicon thin layer, serving as the electrode-to-disk capacitive gap spacing; (b) a second layer of $SiO_2$ (TEOS) is deposited via LPCVD, followed by a combination of CMP and wet $SiO_2$ etch to expose the polysilicon layer; $SiO_2$ dry etch is then performed to etch the second $SiO_2$ (TEOS) layer; (c) 1$^{st}$ and 2$^{nd}$ $SiO_2$ (TEOS) layers as hard mask, resonator disk and side electrodes are then patterned by a Si dry etch, forming an air gap with a nano-scale width determined by the previous polysilicon layer; (d) a back-side $SiO_2$ wet etch is used to remove the remaining $SiO_2$ (TEOS) layer and at the same time to transfer the Si patterns down to the buried $SiO_2$ layer; (e) a thick layer of

photoresist is spun, exposed and developed, not only to remove the undoped polysilicon layer but also to serve as a lift-off mask for the metal film in the following step; (f) a film of metal is plated and patterned by lift-off process; after striping the photoresist and releasing the structure in HF, a final cross section view is yield.

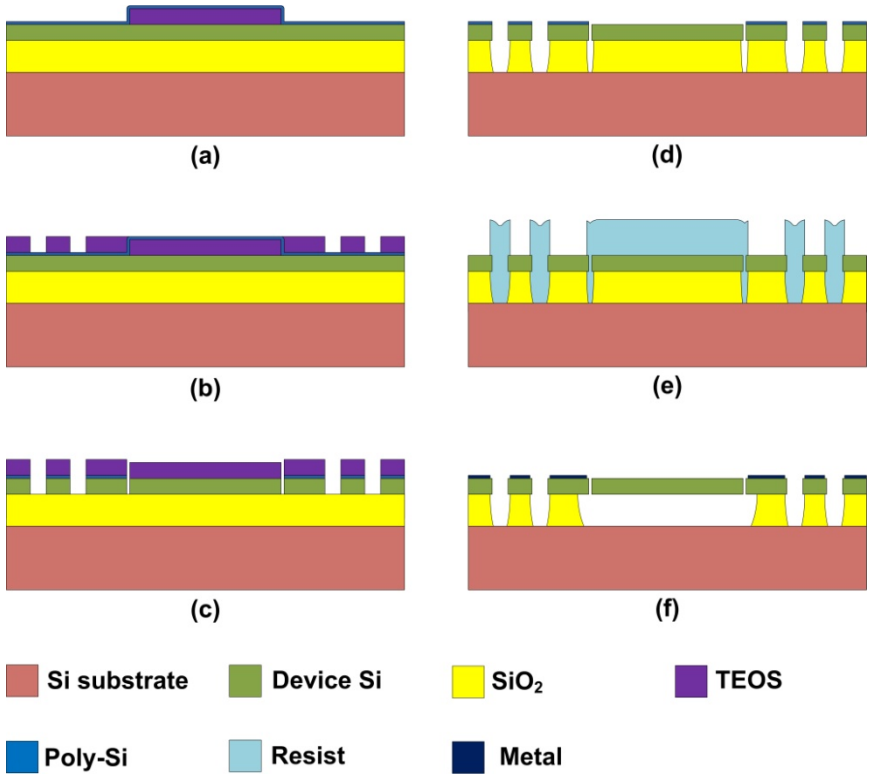


Figure 1.24 Fabrication process flow of the TEOS and CMP based method.

However, currently demonstrated fabrication processes either are very complicated (e.g., HARPSS process) or require nonstandard techniques (e.g., CMP). Moreover, the thickness of the capacitive air gap is limited by the thermal oxidation process and the small dielectric constant of air is not ideal for a capacitive transducer as well. A novel high aspect-ratio SOI micromachining technique is presented in this work that is capable of producing vertical disk resonators and resonator arrays with ultra-thin high-k dielectric solid gap by a simplified process consisting of merely three lithography steps. The detailed processing steps will be discussed in Chapter 3.

## 1.4 Resonator Array

In the ideal case - an array of N resonators, if the resonators are excited at exactly the same resonance frequency, the output current will increase by N times for the same input voltage, thus lowering the motional impedance by N times. Unfortunately, even a tiny frequency mismatch can dramatically affect the combined output. Mechanical coupling provides a superb solution to the frequency-matching problem, which mechanically forces all coupled resonators vibrating at the same frequency as the signal of a given modal resonance frequency applied to the overall resonator array. By means of mechanical coupling and excitation of a parallel array of corner-coupled polysilicon transverse-mode square plate resonators (see Figure 1.25), motional impedance of the "composite" resonator array has been successfully reduced down to 4.4 kΩ at 64 MHz, 4.8 times smaller than the 21.3 kΩ measured by a single square resonator, with $Q > 9000$ [67].

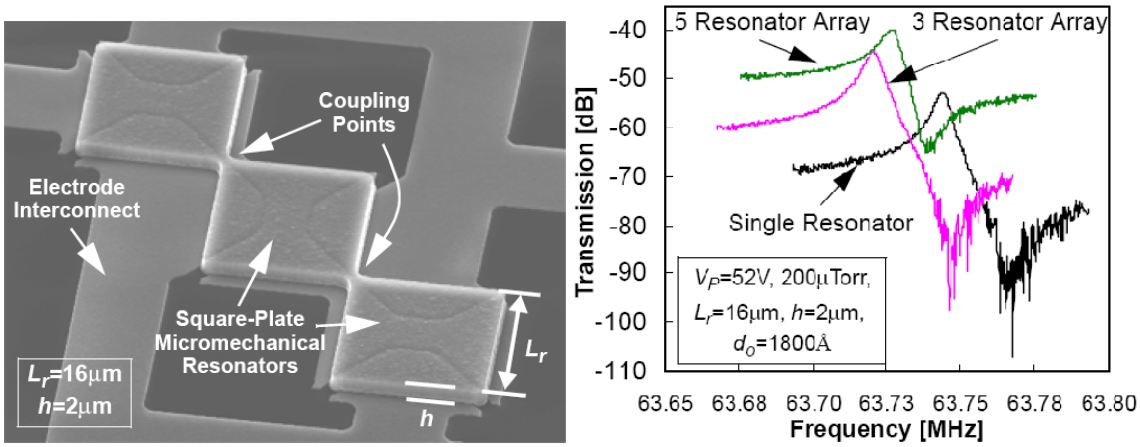


Figure 1.25 SEM image and frequency response spectra of a single and mechanically coupled square resonator arrays with three and five resonators, respectively [67].

### 1.5 Capacitively-Transduced Resonators Using Materials Other than Si

Among the currently available thin-film-depositable materials, diamond offers the best mechanical properties, which has potentials to realize the best the frequency-$Q$ performance. Chemical vapor deposition (CVD) polycrystalline diamond was employed as the material for the resonance disk and polysilicon for the anchoring stem, successfully raising the $Q$ of radial-contour mode disk resonators to 11,555 in vacuum at frequencies of 1.51 GHz [68]. An acoustic impedance mismatch between the two different material suppresses energy transfer from the disk to the stem, thus eliminates anchor losses and leading to a higher $Q$. A MEMS cantilever type resonator exhibited a resonance frequency of 318.2 KHz with $Q$ > 116,000, the highest reported value for a polycrystalline cantilever resonator [69]. Ultra nanocrystalline diamond (UNCD) thin film deposited by hot filament chemical vapor deposition (HFCVD) has been demonstrated, with Young's modulus up to 920 GPa [70], showing a great potential for MEMS resonators to achieve even higher operating frequencies. For applications such as sensing and wireless communication, mechanical resonators with a high $Q$ and high resonance frequency are desirable, as they would lead to the coveted high resolution and high frequency selectivity for sensors and wireless transceivers, respectively. Of course, less energy losses also implies lower power consumption, which is crucial for the portable sensors and wireless transceivers. In addition to the outstanding mechanical strength, diamond as a promising alternative to Si or SiC offers a lot more outstanding properties, such as exceptionally low friction coefficient, excellent thermal stability, great chemical inertness, and very good plasma etching selectivity to Si and $SiO_2$ making micromachining much easier [71].

A comparison of mechanical properties and relevant frequencies among several common MEMS materials is summarized in Table 1.1.

Table 1.1 Properties for different materials and their relevant frequencies.

| Material | Young's Modulus $E$ (GPa) | Density $\rho$ (kg/m$^3$) | Acoustic Velocity (m/s) | Frequency Scaling Factor |
|---|---|---|---|---|
| Polycrystalline Silicon | 150 | 2.33 | 8024 | 1 |
| Silicon or SOI Substrate | 165.7 | 2.33 | 8433 | 1.05 |
| Silicon Carbide | 415 | 3.12 | 11500 | 1.433 |
| Polycrystalline Diamond (800°C-1000°C) | 1144 | 3.5 | 18076 | 2.256 |
| Ultrananocrystalline Diamond (UNCD) (<400°C) | 920 | 3.5 | 16210 | 2.02 |

Material other than commonly used polysilicon, diamond, or single crystalline silicon has also been investigated [72-74]. Some metals have been applied as a main structural material of MEMS resonator by taking the advantage of its low deposition temperature. Particularly, electroplated nickel can be deposited at 40°C-60°C to obtain potentially high aspect radio along with its low cost. With a frequency range from 18 MHz to 426 MHz, electroplated-Ni-based MEMS resonators have been built with $Q$'s of 6,405 and 2,467 in vacuum and in air, respectively [75]. Another attractive benefit from this type of devices is their compatibility to simple fabrication over CMOS circuitry, since the fabrication temperature is lower than 100 ºC, thus making it amenable to post-CMOS MEMS device fabrication [76].

**1.6 Overview**

Despite many efforts being made in past studies for the purpose of reducing motional impedance, using employment of nano-scale high-k solid gap, usage of SOI

substrate and coupling resonators in an array, there has never been sufficient effort in putting all possible techniques together to achieve a optimally low impedance and ultimately to realize a 50 Ω match to the front-end circuitry. A newly-developed fabrication process based on SOI technology utilizes atomic layer deposition (ALD) for formation of nano-scale solid capacitive gap with high-k dielectric material. Through ALD technology, which is capable of providing superb conformability and uniformity as well as outstanding thickness controllability, an ultra-thin layer (~10 nm) is deposited on a high-aspect-ratio feature formed by deep reactive ion etch (DRIE) on SOI, thus allowing the mass production of on-chip capacitively-transduced resonators and resonator arrays with greatly enhanced electromechanical coupling coefficient. The newly developed IC-compatible MEMS microfabrication process consisting of merely three standard photolithography steps, thus showing a great advantage as opposed to other SOI-based resonator device technologies. In addition, the newly developed SOI process allows DC-bias voltage to be directly applied on to the substrate, which ensures the resonator body to be grounded perfectly, thus having a great promise to achieve minimized feed-through capacitance by steering feed-through current to ground. Figure 1.26 illustrates the schematic-view of a 3-by-3 disk resonator array on SOI substrate and the corresponding measurement configuration.

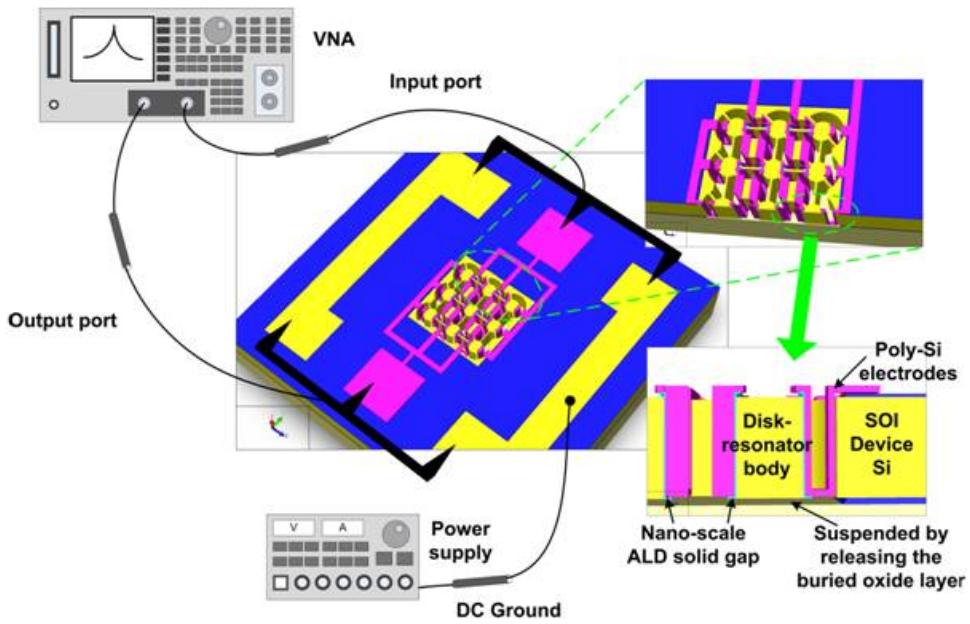


Figure 1.26 Schematic of a 3-by-3 disk resonator array on SOI substrate and its measuring configuration.

Chapter 2 presents a theoretical derivation of wine-glass mode shape of a disk resonator and a ring resonator as well as equivalent circuit models. Chapter 3 details the novel fabrication methodology on SOI substrate. Finally, Chapter 4 concludes this thesis and discusses possible future research directions.

# CHAPTER 2 RESONATOR DESIGN

## 2.1 Extensional Wine-glass Mode and Resonance Frequency Design

### 2.1.1 Wine-glass Mode of a Disk Resonator

Figure 2.1 illustrates key dimensional parameters of a capacitive disk resonator in polar coordinate ($r$, $\theta$) with origin located at the center of the circular plane, which is of radius $R$ anchored by two side-support beams of width $b$ and length $L$. A pair of input/output electrode located on each side of the disk, span an equal angle of $\theta_e$ and separate from the disk by a capacitive gap of $d_s$ and $d_d$ for the sensing (input) and driving (output) electrodes, respectively. The device operates in a two-port bias, excitation and measurement configuration. In order to excite the device into resonance vibration, a direct-current DC-bias $V_p$ is applied to the resonant structure and an AC voltage signal $v_d$ to the driving electrode, generating an electrostatic input force pointing outward from the disk. When the frequency of the input signal $v_d$ matches the wine-glass mode resonance frequency of the disk, the resulting force drives the disk into a elliptic vibrating mode as illustrated by the dot line in Figure 2.1.

The elliptic mode (i.e. wine-glass mode) involves both radial and circumferential displacements, with four nodal points locating at the disk periphery, 90° apart from each other, where the supporting beams are aligned to in order to mitigate the anchor losses. The wine-glass mode generates a DC-biased capacitance between the disk and the output electrode which sources an output current $i_s$. The resonator disk is made of low-resistivity

single crystal silicon, while the input/output electrodes are built with p-type doped polysilicon.

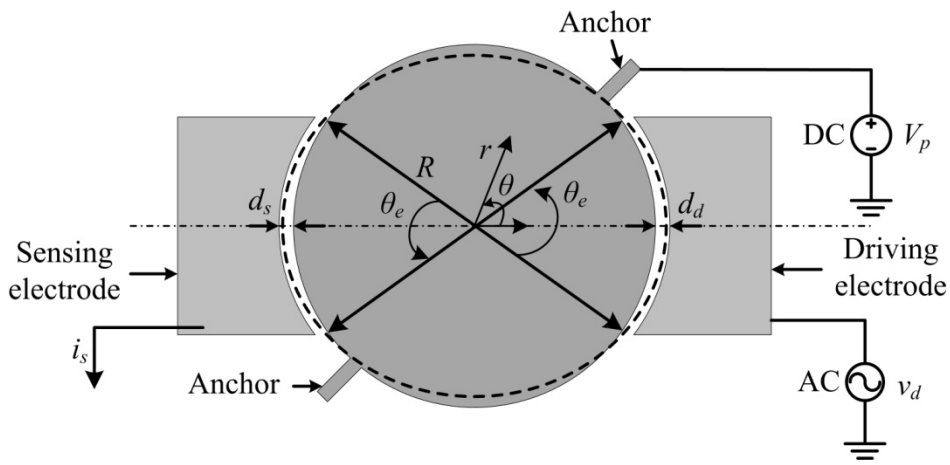


Figure 2.1 Top view of a wine-glass mode disk resonator.

A comprehensive derivation of the in-plane vibration of a disk resonator and the mathematical expression of its mode shape and resonance frequency is provided by this section. Due to the orders of magnitude smaller vertical dimension (i.e. thickness, $h$) of the resonance structure than that of its lateral dimension (i.e. radius, $R$), it may be assumed that the vibration variables are independent of the thickness. In addition, effects of supporting beams on the in-plane vibration can be negligible, if narrow beams are located on the nodal points on the edge of the vibrational disk. Thus the resonator disk can be modeled approximately as an ideal 2-D circular thin plane with free edges, which results in a plane stress scenario.

The differential equation of a 2-D disk in-plane vibration, as derived by Love [77], may be expressed as

$$(\lambda + \mu) \cdot \nabla(\nabla \cdot u) + \mu \cdot \nabla^2 u = \rho \cdot \frac{\partial^2 u}{\partial t^2} \qquad 2.1$$

where $\lambda = E\nu/(1+\nu)(1-2\nu)$ and $\mu = E/2(1+\nu)$ are Lame's constants, $E$, $\nu$, and $\rho$ are Young's modulus, Poisson's ratio, and density of the resonance structure material, respectively. The displacement vector $u$ may be defined in terms of pressure-wave (P-wave) scalar potential, $\Phi$, and shear-wave (S-wave) vector potential, $\Psi$, as [78]

$$u = \nabla\Phi + \nabla \times \Psi \qquad 2.2$$

Combining equation 2.1 and 2.2, the scalar potential, $\Phi$, and the vector potential, $\Psi$, can be written as

$$\frac{\partial^2 \Phi}{\partial t^2} = \alpha^2 \cdot \nabla^2 \Phi \qquad 2.3$$

$$\frac{\partial^2 \Psi}{\partial t^2} = \beta^2 \cdot \nabla^2 \Psi \qquad 2.4$$

where

$$\nabla^2 = \frac{1}{r} \cdot \frac{\partial}{\partial r} + \frac{\partial^2}{\partial r^2} + \frac{1}{r^2} \cdot \frac{\partial}{\partial \theta} \qquad 2.5$$

$$\alpha = \sqrt{\frac{E}{\rho(1-\nu^2)}} \qquad 2.6$$

$$\beta = \sqrt{\frac{E}{2\rho(1+\nu)}} \qquad 2.7$$

$\alpha$, $\beta$ are propagation velocities of the P-wave and S-wave, respectively.

Equation 2.3 and 2.4 may be solved, in terms of the trigonometric and Bessel function. For time-harmonic excitation with time dependence $e^{j\omega_m t}$, the mode shape may be expressed as

$$\Phi_m = A_m \cdot J_m(k_m r / R) \cdot \cos(m\theta) \cdot e^{j\omega_m t} \qquad 2.8$$

$$\Psi_m = B_m \cdot J_m(h_m r / R) \cdot \sin(m\theta) \cdot e^{j\omega_m t} \qquad 2.9$$

where $\omega_m = 2\pi f_m$ is the angular resonance frequency of the $m$-th order, $A_m$ and $B_m$ are constants determined by the excitation amplitude, and $k_m$ and $h_m$ are

$$k_m = \omega_m \cdot R / \alpha \qquad 2.10$$

$$h_m = \omega_m \cdot R / \beta. \qquad 2.11$$

In equation 2.8 and 2.9, $J_m$ is the Bessel's function of first order of the $m$-th order. The mode order, $m$, represents numbers of the nodal diameter in the free vibrational response. When $m$ = 0, the disk resonator entails an axisymmetric uncoupled mode, the displacement is only in the radial direction (radial) or in the circumferential direction (torsional) with no nodal rings. While $m$ = 1 implies a nonzero response at the center point of the disk. Finally, when $m$ is equal to or larger than 2, nodal points on the disk periphery will occur, which are well-suited for attaching the supporting beams to obtain low-loss suspension[79].

By substituting equation 2.8 and 2.9 into 2.2, the time-independent radial ($U$) and circumferential ($V$) components of the displacement, $u$, may be expressed as

$$U_m = \left[ A_m \cdot \frac{d}{dr} J_m(k_m r / R) + \frac{m}{r} B_m \cdot J_m(h_m r / R) \right] \cdot \cos(m\theta) \qquad 2.12$$

$$V_m = \left[ -A_m \cdot \frac{m}{r} J_m(k_m r / R) - B_m \cdot \frac{d}{dr} J_m(h_m r / R) \right] \cdot \sin(m\theta). \qquad 2.13$$

Let $\sigma_r$ and $\tau_{r\theta}$ be the normal and tangential stress at any boundary point of the disk. For a disk with free edge, the stress at the boundary must vanish, namely,

$$\sigma_r \Big|_{r=R} = \frac{E}{1-\nu^2} \cdot \left[ \frac{\partial U}{\partial r} + \frac{\nu}{r} \cdot \left( U + \frac{\partial V}{\partial \theta} \right) \right] = 0 \qquad 2.14$$

$$\tau_{r\theta}\Big|_{r=R} = \frac{E}{2(1+\nu)} \cdot \left[ \frac{\partial V}{\partial r} + \frac{1}{r} \cdot \left( \frac{\partial U}{\partial \theta} - V \right) \right] = 0 \qquad 2.15$$

which leads to the mode frequency equation given by [80]

$$\left[ \frac{k_m \cdot J_{m-1}(k_m)}{J_m(k_m)} - m - \frac{h_m^2}{2(m^2-1)} \right] \cdot \left[ \frac{h_m \cdot J_{m-1}(h_m)}{J_m(h_m)} - m - \frac{h_m^2}{2(m^2-1)} \right] = m^2 \cdot \left[ \frac{h_m^2}{2(m^2-1)} - 1 \right]. \qquad 2.16$$

Substituting Equation 2.12 and 2.13 into 2.14 and 2.15 leads to the following matrix:

$$\begin{bmatrix} a_{11} & a_{12} \\ a_{21} & a_{22} \end{bmatrix} \cdot \begin{bmatrix} A_m \\ B_m \end{bmatrix} = 0 \qquad 2.17$$

which is associated only with $k_m$, $h_m$, and $v$. Thus, the ratio between the constants of $\Phi_m$ and $\Psi_m$ is calculated as:

$$\xi_m = \frac{B_m}{A_m} = \frac{J_m(k_m)}{J_m(h_m)} \cdot \frac{2 \cdot \frac{k_m \cdot J_{m-1}(k_m)}{J_m(k_m)} + h_m^2 - 2m(m+1)}{\left[ \frac{h_m \cdot J_{m-1}(h_m)}{J_m(h_m)} - (m+1) \right] \cdot 2m}. \qquad 2.18$$

From equation 2.12, 2.13, and 2.18, the radial displacement at ($r$, $\theta$) can be written, instead of 2.12 and 2.13, as

$$U = \frac{A_m}{R} \cdot \cos(2\theta) \cdot U_r \qquad 2.19$$

where

$$U_r = k_m \cdot J_{m-1}\left( k_m \cdot \frac{r}{R} \right) - \frac{2R}{r} \cdot J_m\left( k_m \cdot \frac{r}{R} \right) + \frac{2R}{r} \cdot \xi \cdot J_m\left( h_m \cdot \frac{r}{R} \right). \qquad 2.20$$

When $m$ = 2, the disk resonator operates in its wine-glass mode, the dimensionless maximum radial displacement at the disk edge can be expressed as

$$U_R = k \cdot J_1(k_2) - 2J_2(k) + 2\xi \cdot J_2(h). \qquad 2.21$$

Since the capacitive gap is extremely small compared to the size of the disk, the disk-to-electrode configuration can be treated as a parallel plate capacitor. Hence, the electrostatic excitation force for driving and sensing electrode, can be given by [64]

$$F_d(\theta) = \frac{1}{2} \cdot \frac{\varepsilon \cdot h \cdot R}{d_d^2} \cdot \left[ -2 \cdot V_p \cdot v_d + 2 \cdot \frac{A}{R} \cdot \frac{U_R \cdot \cos(2\theta)}{d_d} \cdot V_p^2 \right] \qquad 2.22$$

$$F_s(\theta) = \frac{1}{2} \cdot \frac{\varepsilon \cdot h \cdot R}{d_s^2} \cdot \left[ 2 \cdot \frac{A}{R} \cdot \frac{U_R \cdot \cos(2\theta)}{d_s} \cdot V_p^2 \right] \qquad 2.23$$

where $F_d$, $F_s$, $d_d$, $d_s$ are the electrostatic force and capacitive gaps for the driving and sensing electrodes, respectively, $\varepsilon$ is the permittivity of air, and $A$ denotes $A_m$ ($m = 2$).

For a disk and its side electrodes spanning an angle of $\theta_e$, the electrostatic excitation force for driving and sensing electrodes, can be expressed as

$$\begin{aligned} F_d &= \int_{-\frac{1}{2}\theta_e}^{\frac{1}{2}\theta_e} \left\{ \frac{1}{2} \cdot \frac{\varepsilon \cdot h \cdot R}{d_d^2} \cdot \left[ -2 \cdot V_p \cdot v_d + 2 \cdot \frac{A}{R} \cdot \frac{U_R \cdot \cos(2\theta)}{d_d} \cdot V_p^2 \right] \right\} \\ &= \frac{1}{2} \cdot \frac{\varepsilon \cdot h \cdot R}{d_d^2} \cdot \left[ -2 \cdot V_p \cdot v_d \cdot \theta_e + 2 \cdot \frac{A}{R} \cdot \frac{U_R \cdot \sin(\theta_e)}{d_d} \cdot V_p^2 \right] \end{aligned} \qquad 2.24$$

$$\begin{aligned} F_s &= \int_{-\frac{1}{2}\theta_e}^{\frac{1}{2}\theta_e} \left\{ \frac{1}{2} \cdot \frac{\varepsilon \cdot h \cdot R}{d_s^2} \cdot \left[ 2 \cdot \frac{A}{R} \cdot \frac{U_R \cdot \cos(2\theta)}{d_s} \cdot V_p^2 \right] \right\} \\ &= \frac{1}{2} \cdot \frac{\varepsilon \cdot h \cdot R}{d_s^2} \cdot \left[ 2 \cdot \frac{A}{R} \cdot \frac{U_R \cdot \sin(\theta_e)}{d_s} \cdot V_p^2 \right] \end{aligned} \qquad 2.25$$

It should be noted that the equation 2.16 is solely a function of the Poisson's ratio of the resonance structure material. Given $k_m$ determined by 2.16, the resonance frequency can be calculated by equation 2.10 or 2.11, shown as

$$f_m = \frac{k_m}{2\pi R} \cdot \sqrt{\frac{E}{\rho \cdot \left(1 - \nu^2\right)}} \qquad 2.26$$

where $m \geq 2$.

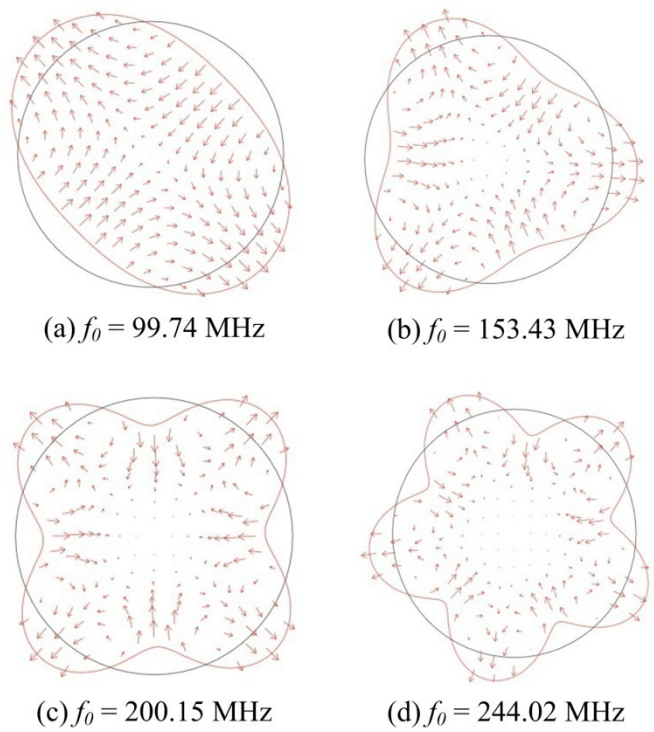


Figure 2.2 Mode shapes and resonance frequency for a 20 μm radius single crystal silicon <100> disk calculated from the theoretical derivation using COMSOL Multiphysics 3.5a with (a) $m$ = 2; (b) $m$ = 3; (c) $m$ = 4; (d) $m$ = 5.

Mode shapes and the corresponding resonance frequencies are obtained by solving equation 2.16 using COMSOL, some of which are shown in Figure 2.2. As illustrated in Figure 2.2, the wine-glass mode shape that we study in this work appears when $m$ =2. The related mechanical parameters of single crystal silicon (SCS) along <100> orientations used in the theoretical derivation are listed in Table 2.1.

Table 2.1 The related parameter for a disk resonator.

| Material | Single crystal silicon <100> | Polysilicon |
|---|---|---|
| Young's modulus ($E$) [Mpa] | 170 | 160 |
| Possion's ratio ($\nu$) | 0.28 | 0.22 |
| Thermal expansion parameter ($\alpha$) [1/K] | 0.0000026 | 0.0000026 |
| Density ($\rho$) [kg/m$^3$] | 2330 | 2320 |

### 2.1.2 Wine-glass Mode of a Ring Resonator

A compound resonance mode design, named "extensional wine-glass resonator", or "EWGR" in [8], which combines two previously demonstrated modes, radial-contour mode [52] and wine-glass mode [51], together with a geometric advantage of a ring structure, is described in this session.

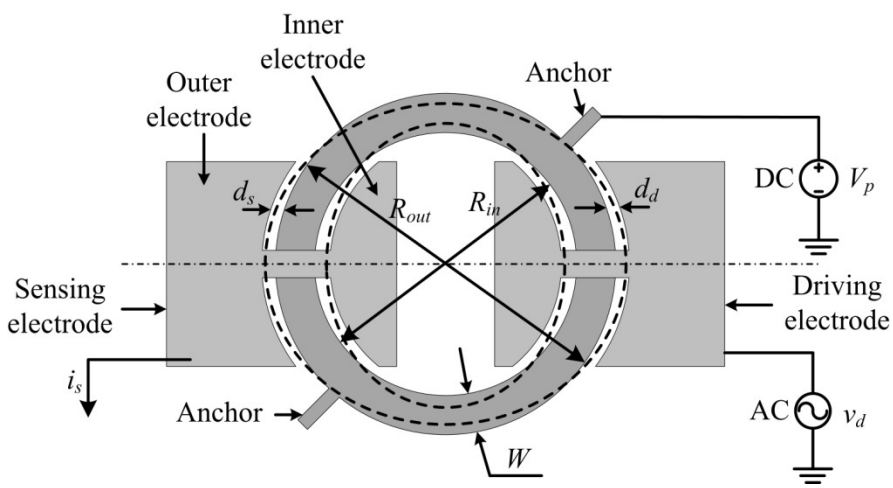


Figure 2.3 Top view of a wine-glass mode ring resonator.

Figure 2.3 illustrates the schematic of a wine-glass mode ring resonator, identifying key dimensions and an excitation configuration. Similar to wine-glass mode disk resonator, the ring resonator is anchored by supporting beams set to the quasinodal points at the ring outer periphery, which minimizes the anchor loss and thus retain the highest $Q$. Electrodes are designed around the ring structure, both inside and outside,

connected by bridges hanging over the resonator body, for the purpose of obtaining the largest transducer overlap capacitance. Excitation mechanism of the ring resonator is similar to the disk resonator. The device firstly converts the input ac signal, $v_d$, to a mechanical force to excite the ring resonator into a modal vibration at the resonance frequency, thus generating a mechanical displacement between the ring structure and side electrodes. The mechanical displacement is then converted back to an electrical signal, sensed by the output electrode. It should be noted that output current is only generated if the dc-bias voltage $V_p$ is finite. When $V_p = 0$ V, the device is effectively "off". Thus, the capacitively-transduced micromechanical resonator with dc bias voltage essentially acts as a switch.

The "EWGR" mode shape consists of four quarter cycles to finish an entire modal vibration cycle. In the first quarter cycle, starting from the original ring shape, the two ring quarters along x-axis gradually expand while the other two quarters along y-axis gradually contract, finally reaching the maximum expansion of the x-axis quarters and maximum contraction of y-axis quarters. Then the motions of the x-axis and y-axis quarters become contraction and expansion, respectively, until reaching the maximum displacement at the end of the first half cycle, as illustrated by the dotted line in Figure 2.3. In the second half cycle, the motion is reversed with the continuing contraction in x-axis quarters and expansion in y-axis quarters. After reaching the maximum displacement, the ring starts to restore towards the original state, finishing the entire cycle. As a result, expansion and contraction is similar to the radial-contour mode vibration, indicating that a high frequency can be achieved, while the displacement of the

inner and outer perimeters of the ring resembles the mode shape of a wine-glass disk, which minimizes anchor-related dissipation to allow high-$Q$ performances.

Figure 2.3 indicates a 2-D ring plate in the cylindrical coordinates ($r$, $\theta$) with origin point at the center of the ring, where the thickness of the ring is much lesser than the inner and outer radius of the ring, whose effect on vibration is negligible while still offering sufficient precision. The time-independent radial and tangential displacement $U_r$ and $U_\theta$ may be expressed as [81]

$$U_r = \frac{1}{h} \cdot \left[ A \cdot \frac{dJ_n(hr)}{dr} + B \cdot \frac{dY_n(hr)}{dr} + \frac{n}{r} \cdot \left( CJ_n(kr) + DY_n(kr) \right) \right] \cos(n\theta) \qquad 2.27$$

$$U_\theta = -\frac{1}{h} \cdot \left[ \frac{n}{r} \cdot \left( AJ_n(hr) + BY_n(hr) \right) + C \cdot \frac{dJ_n(kr)}{dr} + D \cdot \frac{dY_n(kr)}{dr} \right] \sin(n\theta) \qquad 2.28$$

where

$$h^2 = \frac{\rho \cdot \omega_n^2 \cdot \left(1 - \nu^2\right)}{E} \qquad 2.29$$

$$k^2 = \frac{\rho \cdot \omega_n^2 \cdot \left(2 + 2\nu\right)}{E} \qquad 2.30$$

and $\rho$, $E$, and $\nu$ are the density, the Young's modulus, and the Poisson's ratio of the ring structure material, respectively. $\omega_n$ is the $n$-th order angular resonance frequency. $A$, $B$, $C$, $D$ are the constants determined by excitation amplitude.

Boundary conditions at $r = R_{out}$ and $r = R_{in}$ are as follows, due to the zero normal ($\sigma_r$) or tangential ($\tau_{r\theta}$) stress at the free outer and inner ring edges [81]:

$$\sigma_r = \frac{E}{1-\nu^2} \cdot \frac{\partial U_r}{\partial r} + E \cdot \frac{\nu}{1-\nu^2} \cdot \frac{U_r}{r} + \frac{E}{r} \cdot \frac{\nu}{1-\nu^2} \cdot \frac{\partial U_\theta}{\partial \theta} = 0 \qquad 2.31$$

$$\tau_{r\theta} = \frac{E}{2+2\nu} \cdot \left( \frac{\partial U_\theta}{\partial r} + \frac{1}{r} \cdot \frac{\partial U_r}{\partial r} - \frac{U_\theta}{r} \right) = 0 \,. \qquad 2.32$$

Substituting equation 2.20 and 2.21 into 2.22 and 2.23 yields the resonance frequency given by

$$f_0 = \frac{h}{2\pi}\sqrt{\frac{E}{\rho\left(1-\nu^2\right)}} \qquad 2.33$$

where $h$ is a ring geometry-related parameter that satisfies [81]

$$det\ [H_{ij}] = 0 \qquad 2.34$$

where the matrix elements are

$$\begin{aligned}
H_{11} &= \left[\left(kR_{out}\right)^2/2 - n\left(n+1\right)\right]\cdot J_n\left(hR_{out}\right) + hR_{out}\cdot J_{n-1}\left(hR_{out}\right)\\
H_{12} &= \left[\left(kR_{out}\right)^2/2 - n\left(n+1\right)\right]\cdot Y_n\left(hR_{out}\right) + hR_{out}\cdot Y_{n-1}\left(hR_{out}\right)\\
H_{13} &= n\left(n+1\right)\cdot J_n\left(kR_{out}\right) - nkR_{out}J_{n-1}\left(kR_{out}\right)\\
H_{14} &= n\left(n+1\right)\cdot Y_n\left(kR_{out}\right) - nkR_{out}Y_{n-1}\left(kR_{out}\right)\\
H_{21} &= \left[\left(kR_{in}\right)^2/2 - n\left(n+1\right)\right]\cdot J_n\left(hR_{in}\right) + hR_{in}\cdot J_{n-1}\left(hR_{in}\right)\\
H_{22} &= \left[\left(kR_{in}\right)^2/2 - n\left(n+1\right)\right]\cdot Y_n\left(hR_{in}\right) + hR_{in}\cdot Y_{n-1}\left(hR_{in}\right)\\
H_{23} &= n\left(n+1\right)\cdot J_n\left(kR_{in}\right) - nkR_{in}J_{n-1}\left(kR_{in}\right)\\
H_{24} &= n\left(n+1\right)\cdot Y_n\left(kR_{in}\right) - nkR_{in}Y_{n-1}\left(kR_{in}\right)\\
H_{31} &= nkR_{out}J_{n-1}\left(hR_{out}\right) - n\left(n+1\right)\cdot J_n\left(hR_{out}\right)\\
H_{32} &= nkR_{out}Y_{n-1}\left(hR_{out}\right) - n\left(n+1\right)\cdot Y_n\left(hR_{out}\right)\\
H_{33} &= -kR_{out}\cdot J_{n-1}\left(kR_{out}\right) + \left[n\left(n+1\right) - \left(kR_{out}\right)^2/2\right]\cdot J_n\left(kR_{out}\right)\\
H_{34} &= -kR_{out}\cdot Y_{n-1}\left(kR_{out}\right) + \left[n\left(n+1\right) - \left(kR_{out}\right)^2/2\right]\cdot Y_n\left(kR_{out}\right)\\
H_{41} &= nkR_{in}J_{n-1}\left(hR_{in}\right) - n\left(n+1\right)\cdot J_n\left(hR_{in}\right)\\
H_{42} &= nkR_{in}Y_{n-1}\left(hR_{in}\right) - n\left(n+1\right)\cdot Y_n\left(hR_{in}\right)\\
H_{43} &= -kR_{out}\cdot J_{n-1}\left(kR_{in}\right) + \left[n\left(n+1\right) - \left(kR_{in}\right)^2/2\right]\cdot J_n\left(kR_{in}\right)\\
H_{44} &= -kR_{in}\cdot Y_{n-1}\left(kR_{in}\right) + \left[n\left(n+1\right) - \left(kR_{in}\right)^2/2\right]\cdot Y_n\left(kR_{in}\right)
\end{aligned} \qquad 2.35$$

where $R_{in}$ and $R_{out}$ are the inner and outer radius of the ring, respectively, $J_n$ and $Y_n$ are the Bessel function of the first and second kind, and $n$ is the circumferential order of the mode shape.

Considering the extensional wine-glass mode of a ring resonator is basically the expansion and contraction in the ring width, which is similar to the longitudinal vibration of a bar, the resonance frequency, thus, can be approximately expressed as [8]

$$f_{0approx} = \frac{n}{2W}\sqrt{\frac{E}{\rho}},\ m = 1, 3, 5, \cdots \qquad 2.36$$

where $W = R_{out} - R_{in}$ is the width of the ring, and $n$ is the order of the mode shape.

## 2.2 Equivalent Circuit Model

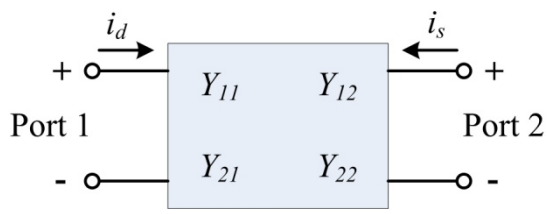


Figure 2.4 The two-port electrical circuit model represented by *Y*-parameters.

A model describing the admittance parameters (*Y*-parameters) of a micromechanical disk resonator is developed to aid in analysis and design of the device. As shown in Figure 2.4, four *Y*-parameters in the two-port equivalent circuit model are defined as the ratio of the current measured at one port to the voltage at the driving port while short-circuiting the undriven port [82], expressed as

$$\begin{aligned} Y_{11}(j\omega) &= \left.\frac{i_d(j\omega)}{v_d(j\omega)}\right|_{v_s=0}, Y_{12}(j\omega) = \left.\frac{i_d(j\omega)}{v_s(j\omega)}\right|_{v_d=0} \\ Y_{21}(j\omega) &= \left.\frac{i_s(j\omega)}{v_d(j\omega)}\right|_{v_s=0}, Y_{22}(j\omega) = \left.\frac{i_s(j\omega)}{v_s(j\omega)}\right|_{v_d=0} \end{aligned} \qquad 2.37$$

Equation 2.37 can be expressed as the product of the mechanical force-displacement transfer function, $Z(j\omega)/F(j\omega)$, the electromechanical coupling at the input and output ports, $\eta_1$, $\eta_2$, $\eta_1'$, and $\eta_2'$, where $\eta_1$ and $\eta_2$ denotes the electromechanical coupling from the driving electrode to the sensing electrode, while $\eta_1'$ and $\eta_2'$ denote the

coupling from the sensing electrode to the driving electrode. The input and output coupling terms can be expressed as [83]

$$\eta_1(j\omega) = \frac{F(j\omega)}{v_d(j\omega)} \tag{2.38}$$

$$\eta_2(j\omega) = \frac{Q_s(j\omega)}{Z(j\omega)} = \frac{1}{j\omega} \cdot \frac{i_s(j\omega)}{Z(j\omega)} \tag{2.39}$$

$$\eta_1'(j\omega) = \frac{Q_d(j\omega)}{Z(j\omega)} = \frac{1}{j\omega} \cdot \frac{i_d(j\omega)}{Z(j\omega)} \tag{2.40}$$

$$\eta_2'(j\omega) = \frac{F(j\omega)}{v_s(j\omega)} \tag{2.41}$$

where $Q_s$ and $Q_d$ are the charge going through the driving and sensing electrode, respectively, and the displacement $Z$ here denotes the vibration amplitude $A/R$. By combining the above equations, $Y_{11}$ and $Y_{21}$ may be rewritten as [83]

$$Y_{11}(j\omega) = \frac{Z(j\omega)}{F(j\omega)} \cdot \frac{F(j\omega)}{v_d(j\omega)} \cdot \frac{i_d(j\omega)}{Z(j\omega)} = j\omega \cdot \frac{Z(j\omega)}{F(j\omega)} \cdot \eta_1 \cdot \eta_1' \tag{2.42}$$

$$Y_{21}(j\omega) = \frac{Z(j\omega)}{F(j\omega)} \cdot \frac{F(j\omega)}{v_d(j\omega)} \cdot \frac{i_s(j\omega)}{Z(j\omega)} = j\omega \cdot \frac{Z(j\omega)}{F(j\omega)} \cdot \eta_1 \cdot \eta_2. \tag{2.43}$$

To determine the resonator admittance, three terms on the right side of equation 2.42 and 2.43 must be expressed in terms of the electromechanical properties of the resonator.

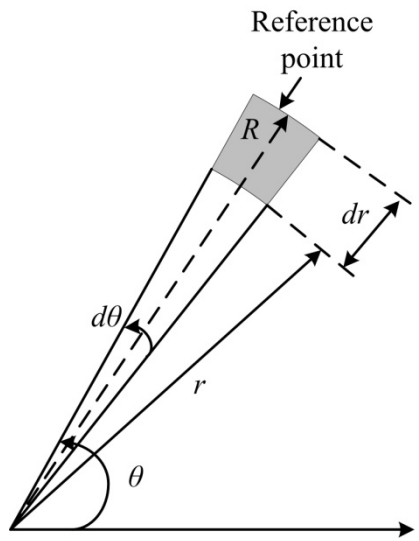


Figure 2.5 An infinitesimal element $d\theta$ along the circumferential direction $\theta$.

As illustrated in Figure 2.5, along the circumferential direction, $\theta$, as the reference point, the effective mass for an infinitesimal element, $d\theta$, may be expressed as [64]

$$m(d\theta) = \rho \cdot h \cdot R^2 \cdot \Sigma / U_R^2 \cdot d\theta \qquad 2.44$$

where $\Sigma = \int_0^1 U_r^2 \cdot \frac{r}{R} \cdot dr'$ is the integral for the kinetic energy.

The dynamic behavior of the infinitesimal element can be described by the second-order equation of motion**,** as

$$\left\{ m(\theta) \cdot \frac{d^2}{dt^2}\left[\frac{A}{R} \cdot U_R\right] + c_d \cdot \frac{d}{dt}\left[\frac{A}{R} \cdot U_R\right] + K(\theta) \cdot \left[\frac{A}{R} \cdot U_R\right] \right\} \cdot \cos(2\theta) = f_e(\theta) \qquad 2.45$$

where $c_d$ is the damping-related coefficient for the infinitesimal element and $f_e(\theta)$ is the radial electrostatic force per unit radian. Multiplying 2.45 by the mode shape, $\cos(2\theta) \cdot U_R$ and integrating from 0 to 2π, gives rise to

$$\pi \cdot \rho \cdot h \cdot R^2 \cdot \frac{\sum}{U_R^2} \cdot \frac{d^2}{dt^2}\left[\frac{A}{R}\right] + C_d \frac{d}{dt}\left[\frac{A}{R}\right] + \pi \cdot \rho \cdot h \cdot R^2 \cdot \frac{\sum}{U_R^2} \cdot \omega^2 \cdot \frac{A}{R}$$
$$= \frac{1}{U_R} \cdot \int_0^{2\pi} f_e(\theta) \cdot \cos(2\theta) \cdot d\theta \qquad 2.46$$

where $C_d$ is the damping-related coefficient of the disk resonator. Thus, the equivalent mass and equivalent stiffness, respectively, can be expressed as

$$M = \pi \cdot \rho \cdot h \cdot R^2 \cdot \sum / U_R^2 \qquad 2.47$$

$$K = M \cdot \omega^2 \qquad 2.48$$

The equivalent electrostatic stiffness and the equivalent force for wine-glass mode disk resonator, by substituting the electrostatic excitation force calculated in 2.24 and 2.25 to 2.46, may be expressed as

$$K_e = \varepsilon \cdot h \cdot R \cdot \left(\frac{\theta_e}{2} + \frac{\sin(2\theta_e)}{4}\right) \cdot V_p^2 \cdot \left(\frac{1}{d_d^3} + \frac{1}{d_s^3}\right) \qquad 2.49$$

$$F = \frac{\varepsilon \cdot h \cdot R}{d_d^2 \cdot U_R} \cdot \left(-V_p \cdot v_d\right) \cdot \sin(\theta_e). \qquad 2.50$$

Hence, the equivalent mechanical model for the disk resonator can be written by

$$M \cdot \frac{d^2}{dt^2}\left[\frac{A}{R}\right] + C_d \cdot \frac{d}{dt}\left[\frac{A}{R}\right] + \left(K - K_e\right) \cdot \frac{A}{R} = F. \qquad 2.51$$

From 2.51, the first term of the admittance parameter equation (i.e. the force-displacement transfer function of the resonator), can be determined via modal analysis, which is

$$\frac{Z(j\omega)}{F(j\omega)} = \frac{\dfrac{1}{K \cdot j\omega}}{\dfrac{j\omega}{\omega^2} + \dfrac{1}{\omega \cdot Q} + \left(1 - K_e/K\right) \cdot \dfrac{1}{j\omega}} \qquad 2.52$$

where $Q$ is the quality factor of the disk resonator.

Substituting 2.51 to 2.38 and 2.41, the coupling of the input and output electrodes can be written as [64]:

$$\eta_1(j\omega) = \frac{\varepsilon \cdot h \cdot R}{d_d^2 \cdot U_R} \cdot (-V_P) \cdot \sin(\theta_e) \qquad 2.53$$

$$\eta_2(j\omega) = \frac{\varepsilon \cdot h \cdot R}{d_d^2} \cdot U_R \cdot (-V_P) \cdot \sin(\theta_e) \qquad 2.54$$

$$\eta'(j\omega) = \frac{\varepsilon \cdot h \cdot R}{d_s^2} \cdot U_R \cdot (-V_P) \cdot \sin(\theta_e). \qquad 2.55$$

$$\eta_2'(j\omega) = \frac{\varepsilon \cdot h \cdot R}{d_s^2 \cdot U_R} \cdot (-V_P) \cdot \sin(\theta_e). \qquad 2.56$$

Similarly, $Y_{12}$ and $Y_{22}$ can be derived, expressed as

$$Y_{12} = Y_{21} = Y_{11}\frac{\eta_2}{\eta_1'} = Y_{22}\frac{\eta_1'}{\eta_2}. \qquad 2.57$$

Substituting 2.52- 2.56 to 2.42 and 2.43 gives rise to the transfer function in the form of *Y*-parameters of a series *RLC* tanks with the equivalent inductance, capacitance, and resistance expressed as, respectively [64]

$$L_{21} = \frac{K}{\eta_1 \cdot \eta_2 \cdot \omega^2} \qquad 2.58$$

$$C_{21} = \frac{\eta_1 \cdot \eta_2}{K \cdot (1 - K_e/K)} \qquad 2.59$$

$$R_{21} = \frac{\sqrt{K \cdot M}}{Q \cdot \eta_1 \cdot \eta_2} \qquad 2.60$$

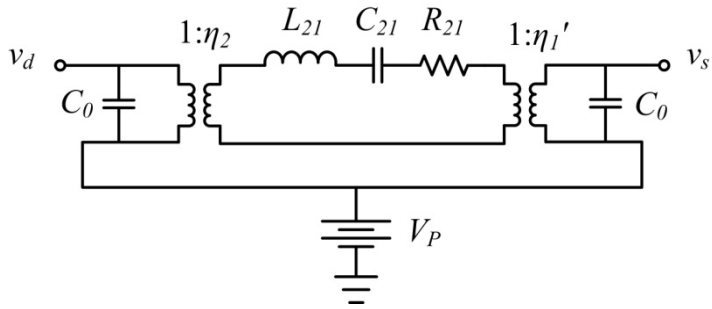


Figure 2.6 Electrical equivalent circuit model for a two-port disk resonator.

Note that $R_{21}$ is commonly referred to the motional resistance. Therefore, the electrical equivalent circuit model of a two-port disk resonator may be derived as shown in Figure 2.6 where $C_0$ represents the electro-to-resonator overlap capacitance.

# CHAPTER 3 MICROFABRICATION PROCESS OF THE WINE-GLASS MODE DISK RESONATOR AND ARRAY ON SOI SUBSTRATE

## 3.1 Microfabrication Process on SOI Substrate

Given the advantages of utilizing SOI substrate described in Chapter 1, the fabrication process is designed to reduce the complicity associated with SOI substrate while producing the best performance of the resonator device. Particularly, instead of solely applying dc-bias to the resonator body, the whole substrate is grounded in this process, allowing the possibility of minimized feed-through capacitance. A layer of boron-doped poly-Si is deposited serving as the electrodes for ac input and output, isolated from dc by a composite film of thermally grown $SiO_2$ and ALD high-k dielectric as shown in Figure 3.1.

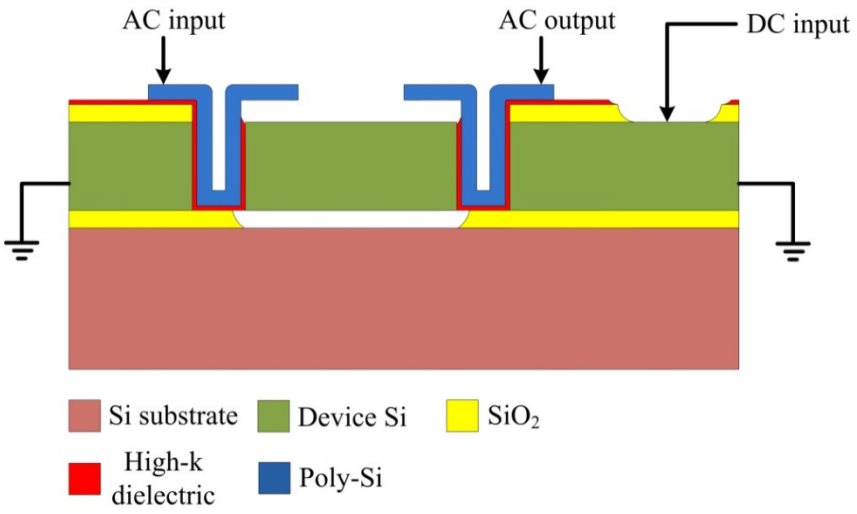


Figure 3.1 Cross-section view of a single wine-glass disk resonator on SOI substrate.

The fabrication process of the wine-glass mode resonator on SOI substrate is based on bulk micromachining and surface micromachining, including substrate etching,

several thin film deposition steps and selective removal of thin films. The entire process flow is illustrated in Figure 3.2 in cross-sectional view.

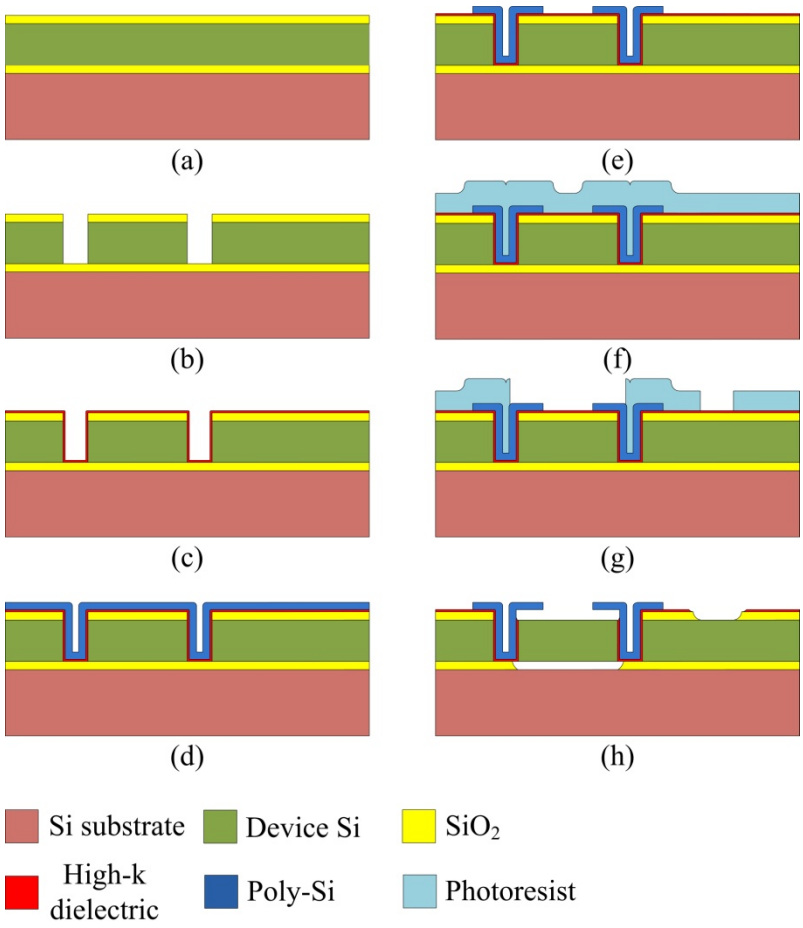


Figure 3.2 Cross-section view process flow of a wine-glass disk resonator on SOI substrate.

Starting with a SOI wafer, a 1.5 μm thick layer of $SiO_2$ is grown by wet oxidation on the SOI wafer. AZP4620 photoresist is used for the 1st photolithography step due to its high resistibility to plasma etch. The resist patterns are then transferred to the $SiO_2$ layer by deep reactive ion etch (DRIE) (AMS 100, Alcatel Micro Machining Systems) using the $CH_4/C_4F_8$ chemistry. With the patterned $SiO_2$ layer as hard mask, the device Si layer

is etched by Si DRIE that employs Bosch process [84] with buried $SiO_2$ as a stopping layer, yielding the schematic view and SEM image in Figure 3.3.

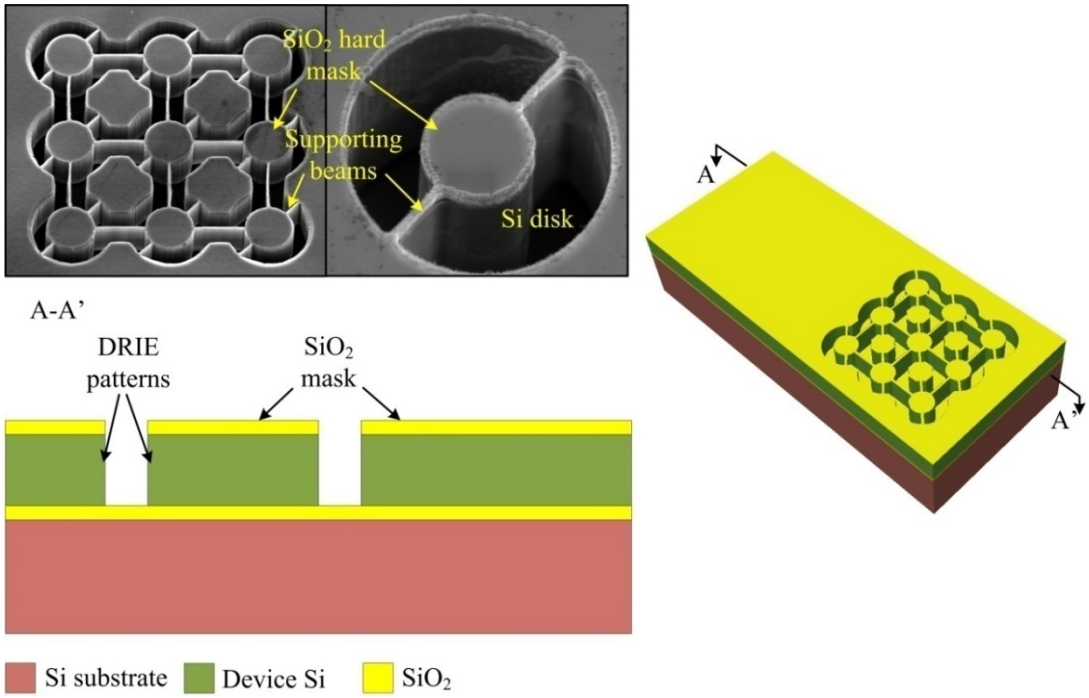


Figure 3.3 SEM, cross-section, and 3-D schematic view after the 1st lithography step and Si DRIE to define the resonator body structure.

After patterning the resonator structure by DRIE process, a layer of 10 nm-20 nm $HfO_2$ is deposited to serve as the high-k dielectric solid gap between the disk resonator body and surrounding electrodes. ALD deposition using Savannah™ S100 system from Cambridge Nanotech was used to deposit $HfO_2$ at 200°C with $Hf(NMe_2)_4$ (Strem Chemicals Inc., 99.99%) and $H_2O$ used as the precursors. The substrate was alternatively exposed to $Hf(NMe_2)_4$ and water vapor that were carried by nitrogen flow for a desired cycle number with 0.9 Å/cycle deposition rate. The $HfO_2$ film is then annealed in $N_2$ atmosphere at 800°C for 5 minutes for the purpose of reducing its etch rate in HF solution used to remove the buried $SiO_2$ layer and release the resonator structure.

Following the ALD process, 2 μm of poly-silicon is deposited via LPCVD at 605°C and then doped by boron–nitride solid source at 1050°C, achieving $R_s$ of 20~30 Ω/sq. To define the electrodes, a layer of SU-8 3025 photoresist is next spun 30 μm-thick to completely submerge the poly-silicon topography deep under the quasi-planarized photoresist film. After exposing and developing the photoresist, the poly-silicon electrodes are patterned via a combined dry and wet Si etch to yield the cross-section shown in Figure 3.4.

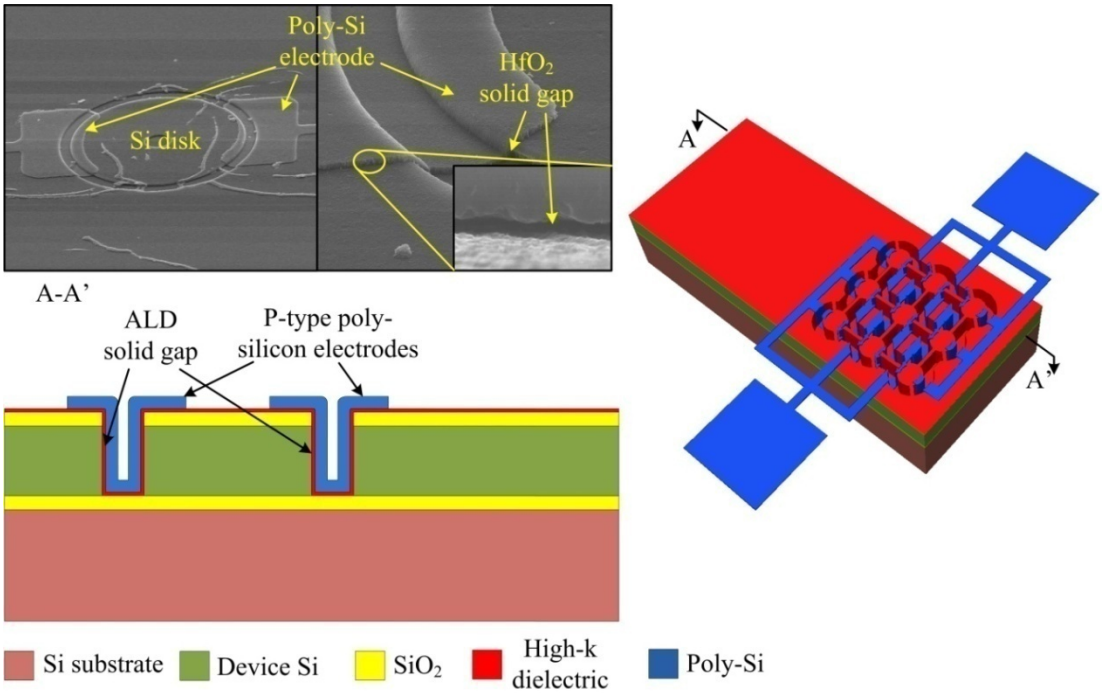


Figure 3.4 SEM, cross-section and 3-D view after the 2nd lithography step and Si etch to define the electrodes.

A subsequent (3rd mask) layer of photoresist is spun, exposed and developed, for the purpose of releasing the resonator structure as well as opening via to the dc bias substrate. After soaking in 49% concentrated HF, the final cross-section of Figure 3.5 is formed. During the releasing step, the high-k dielectric capacitive solid gap is well protected because of two main reasons: (1) it is very difficult for the HF to enter the nm-

scale gap spacing while a large area of $SiO_2$ is exposed directly towards the solution; (2) $N_2$ annealing makes the etch rate of $HfO_2$ much lower than that of $SiO_2$.

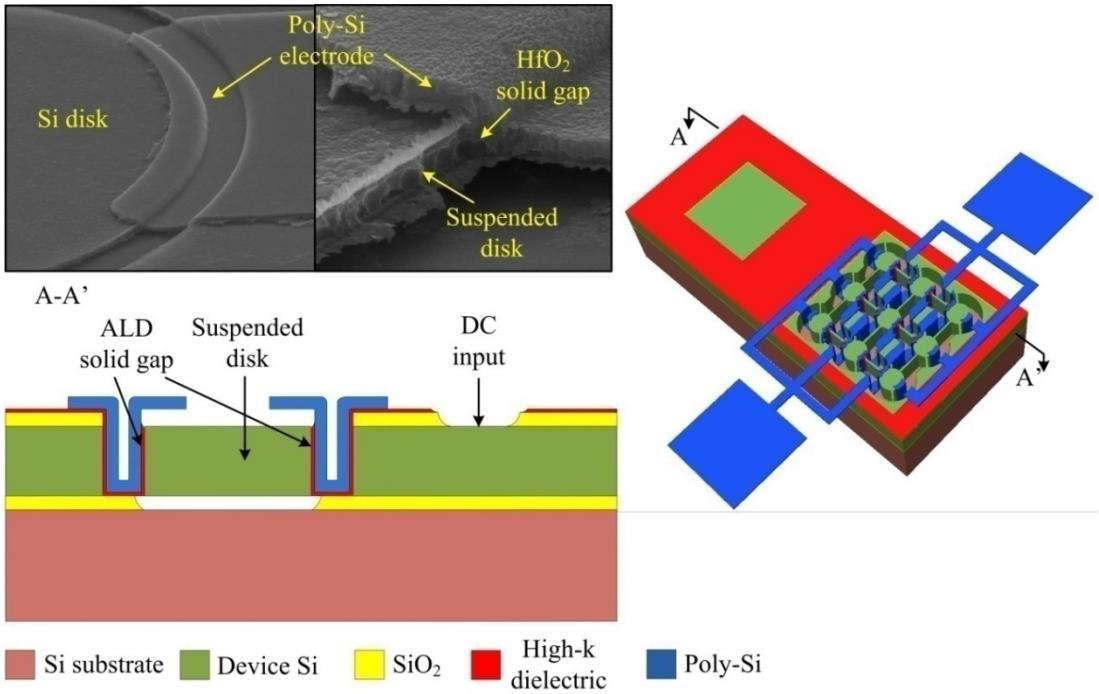


Figure 3.5 SEM image, cross-section and 3-D view of the final device.

### 3.2 High-Aspect-Ratio Si DRIE

DRIE is one of the most important and popular techniques among the options for fabricating high aspect ratio structures (HARS) in silicon. The Bosch process, also called time multiplexed deep etching (TMDE), successfully fulfils the requirements of HARS: high etch rate, good selectivity to masking material, anisotropy, and compatibility with other processes. The basic etching mechanism is based on etch/deposition cycle to allow silicon anisotropic etching by cycling $SF_6$ and $CF_4$ gases, as illustrated in Figure 3.6.

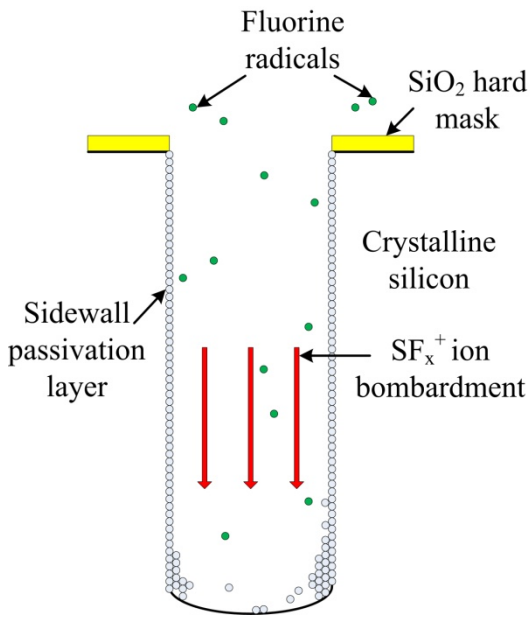


Figure 3.6 Schematic view of Bosch process principle.

Single crystal silicon can be etched by any halogen atoms, such as F, Cl, Br, I, but only can react with F atoms spontaneously:

$$Si_{(s)} + 4F_{(g)} \Rightarrow SiF_4 + \Delta G_0$$

$SF_6$ is used in Bosch process to create F radicals while being dissociated in plasma:

$$SF_6 \rightarrow SF_5^* + F$$

Silicon etch rate depends on the available F partial pressure and on the area of silicon to be removed. However, the etching of silicon in F chemistry is pure isotropic, hence another gas is essential to provide protection to the side walls. $C_4F_8$ is dissociated to -($CF_2$)- species able to react with Si to create the polymer protecting the Si side walls. In the meantime, the polymer deposition on the mask can improve the mask selectivity. To sum up, $SF_6/C_4F_8$ cycling reactions in Bosch process can be expressed as:

Etching: $Si + 4F^* \rightarrow SiF_4$ (volatile molecule)

Passivation: $-(CF_2)- \rightarrow -(CF_2)-n$ (Teflon like material),

as shown in Figure 3.7.

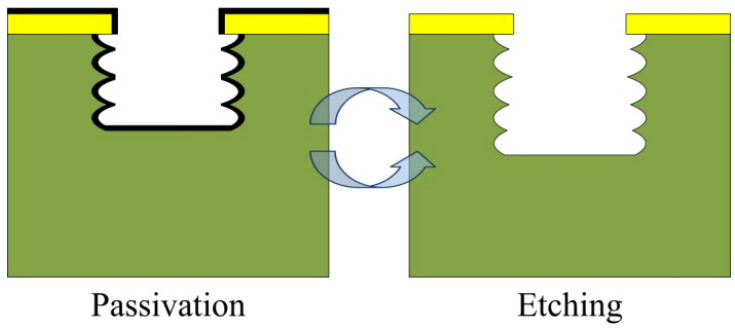


Figure 3.7 Schematic view graph of the two-step Bosch process.

The Si DRIE recipe used in this work is listed in Table 3.1. A small portion of $O_2$ is added to $C_4F_8$ in order to achieve higher aspect ratio. During the passivation step, very weak $O_2$ plasma is formed and a small amount of deposited polymer can be removed, thus increasing Si etch rate and aspect ratio while keeping the selectivity in a good range.

Table 3.1 Different Si DRIE recipe used in this work.

| Recipe | Cycle | | | | Source power (w) |
|---|---|---|---|---|---|
| | Etching | | Passivation | | |
| | $SF_6$ flow rate (sccm) | $SF_6$ pulse time (s) | $C_4F_8/O_2$ flow rate (sccm) | $C_4F_8/O_2$ pulse time (s) | |
| A | 300 | 3 | 200/20 | 1.4 | 2400 |
| B | 300 | 3 | 200/21 | 1.4 | **2000** |
| C | 300 | **2.6** | 200/22 | 1.4 | 2400 |
| D | 300 | 3 | 200/23 | **1.8** | 2400 |

A simplified physical model can be used to simulate the Bosch process. As illustrated in Figure 3.8, for a complete deposition/etch cycle, within the deposition time of $t_1$, a thin layer of polymer with a thickness of $a_1 \cdot t_1$ is deposited, where $a_1$ is the polymer deposition rate. In the etch step with a time of $t_2$, the first portion of $t_2$ is used to

remove the polymer deposited on the bottom of the feature and the rest of $t_2$ is spent on silicon etch, which can be expressed as

$$t = t_2 - \frac{a_1 \cdot t_1}{a_2}, \qquad 3.1$$

where $a_2$ is the polymer removal rate.

Given the isotropic Si etch rate of $a_3$, the etch depth achieved during one deposition/etch cycle can be written as

$$L = a_3 \cdot t = a_3 \cdot \left(t_2 - \frac{a_1 \cdot t_1}{a_2}\right), \qquad 3.2$$

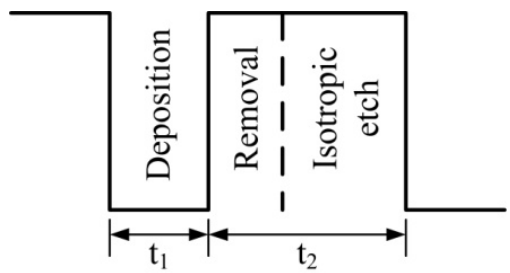


Figure 3.8 A simplified model for the Bosch process: in one deposition/etch cycle, the deposition step lasts for a period of $t_1$, and the etch step for $t_2$, which includes both polymer removal and Si isotropic etch.

Therefore, an oxygen plasma cleaning process is required at the end of each etch to remove the passivation layer deposited on the sidewalls of the DRIE patterned SEM image of Figure 3.9(a) shows the evidence of polymer accumulation on Si sidewalls after DRIE, and Figure 3.9(b) is taken from the same sample after 10 min oxygen plasma cleaning process. As seen, residues on the sidewall are removed in oxygen plasma.

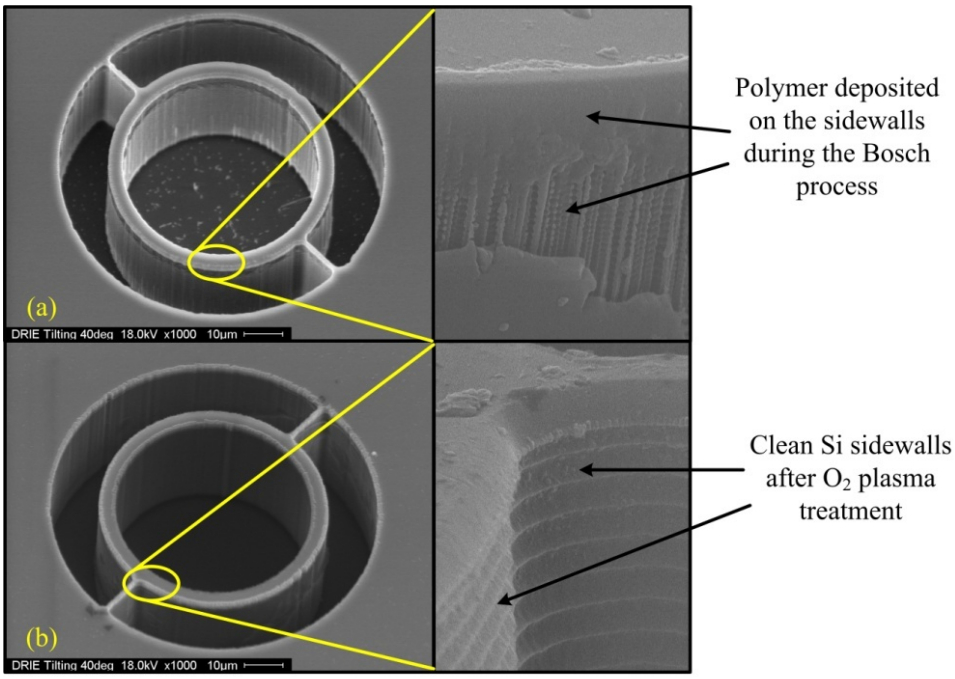


Figure 3.9 SEM photos of DRIE Si sidewalls (a) before and (b) after oxygen plasma treatment.

High aspect-ratio DRIE is an essential step that enables fabrication of many MEMS devices such as high precision motion sensors [85, 86] and high performance low motional capacitively-transduced resonators [55, 87]. In these applications, trench aspect-ratio, sidewall smoothness and trench profile are amongst the critical process parameters. Optimization of these parameters will be discussed in detail in the following sections.

### 3.2.1 Etch Rate

From equation 3.2 the etch rate can be increased in several ways. First, the overall Si etch rate can be increased by increasing the isotropic Si etch rate $a_3$, which can be realized by increasing the ICP source power, $SF_6$ gas flow rate and pulse time. Second, if step time is fixed, the overall etch rate can also be increased by reducing the polymer deposition rate $a_1$, which can be realize by decrease $C_4F_8$ flow rate and duration time.

For the purpose of obtaining better sidewall smoothness and better control of the trench thickness, the etch rate of 8~9 μm/min of the original recipe (see Table 3.1) needs to be reduced. The effect of source power, $SF_6$ pulse time and $C_4F_8/O_2$ pulse time on Si etch rate have been studied independently. The Si etch rate decreased as the source power or $SF_6$ pulse time reduced and $C_4F_8/O_2$ pulse time increased, which shows a perfect match to equation 3.2 as illustrated in Figure 3.10.

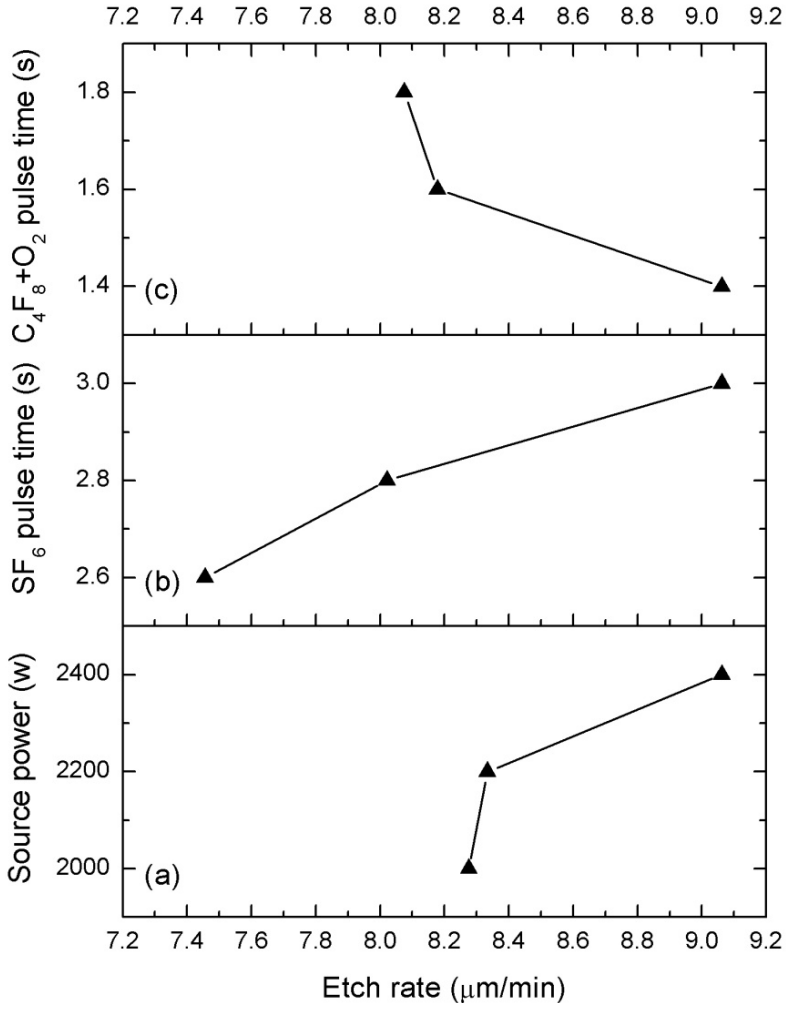


Figure 3.10 Si etch time vs. (a) source power, (b) $SF_6$ pulse time, and (c) $C_4F_8/O_2$ pulse time.

### 3.2.2 Sidewall Smoothness

One limitation of Bosch process is the sidewall "scalloping" formed due to etch/deposition cycle. The scallop size, i.e. peak-to-peak dimension, is the etch depth achieved during etching step in one cycle, *L*, suggesting that the scallop size is directly linked to the Si etch rate. Thus high etch rate is often achieved at the expense of rougher sidewalls in Bosch process.

As demonstrated in section 3.2.1, Si etch rate decreases when source power, $SF_6$ pulse time increases and $C_4F_8/O_2$ pulse time decreases. SEM images in Figure 3.11 shows a reduction of scalloping size when the Si DRIE recipes (i.e. recipe B, C, and D shown in Table 3.1) is modified to realize lower etch rate.

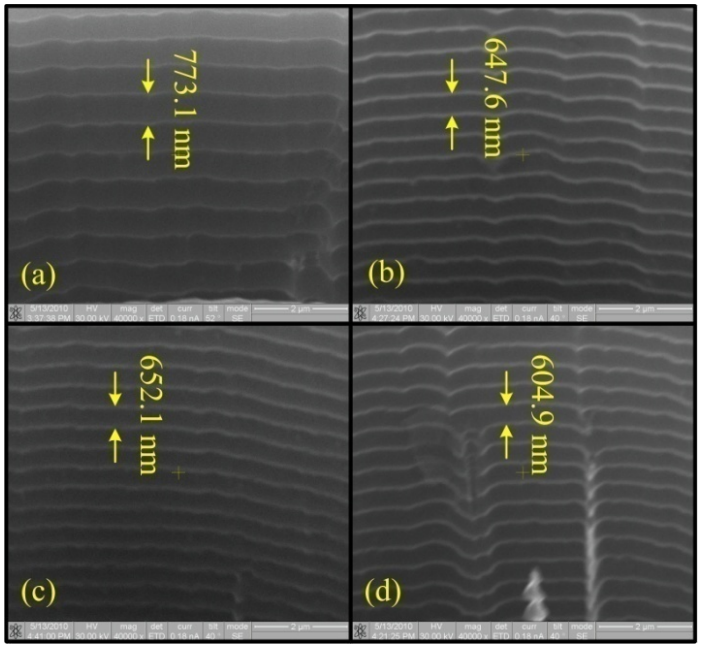


Figure 3.11 SEM photos of Si sidewall scalloping formed by different Si DRIE recipes: (a) original recipe A; (b) recipe B with reduced source power; (c) recipe C with reduced $SF_6$ pulse time; (d) recipe D with increased $C_4F_8/O_2$ pulse time.

### 3.2.3 Aspect Ratio Dependent Etching (ARDE)

MEMS devices usually have structures with different dimensions and aspect ratios that coexist on a single microchip. However, Si etching is aspect ratio dependent, which can be manifested in two ways: first, for a specific feature, etch rate decreases as the aspect ratio increases over time; second, for features with different dimensions, etch rate is higher of wider features than narrower features.

The Si etch rate decreases when etch time increases, which dropped from ~ 10 μm/min in a 1 min etch to ~ 7.5 μm/min in a 9 min one, as depicted in Figure 3.12. The etch rate reduction could be caused by insufficient passivation layer etching during a deposition/etch cycle. Therefore, the polymer deposited at the bottom of the etched trenches accumulates as the etch time increases, leading to a longer polymer removal step time and a shorter Si isotropic etch step time, thus a reduced Si etch rate.

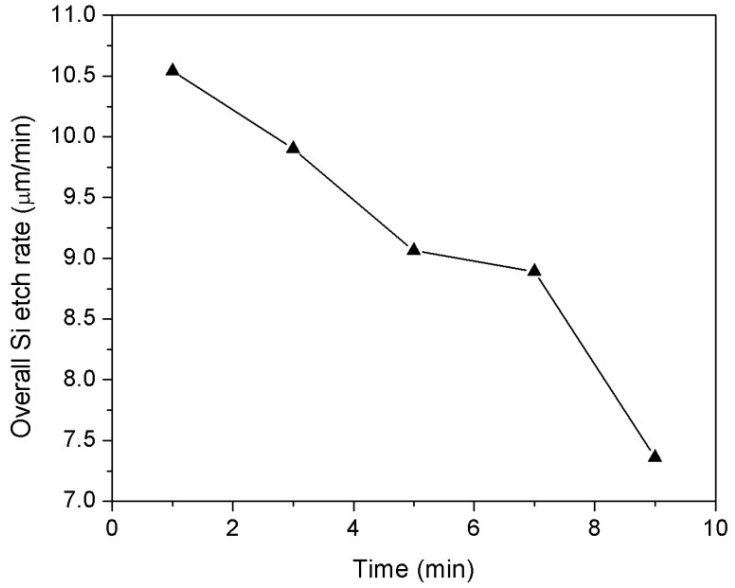


Figure 3.12 Overall Si etch rate decreases with increasing etch time.

In addition, as the aspect ratio of the trench increases, effective removal of the passivation layer becomes more crucial mainly because of the decayed ion flux down to

the bottom of the trench (see Figure 3.13). Hence, the Si etch rate decreases as the trench dimension decreases.

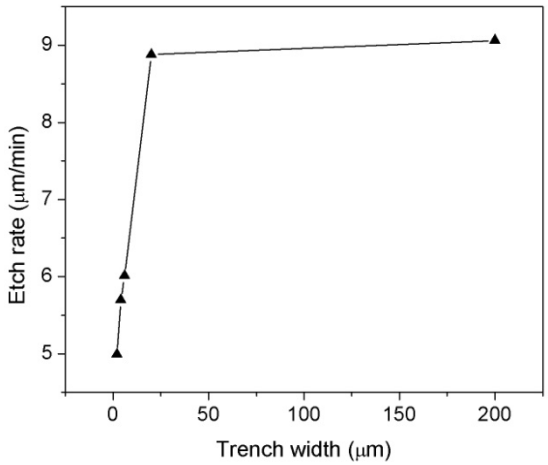


Figure 3.13 Si etch rate decreases dramatically as aspect ratio increases.

### 3.3 Atomic Layer Deposition (ALD)

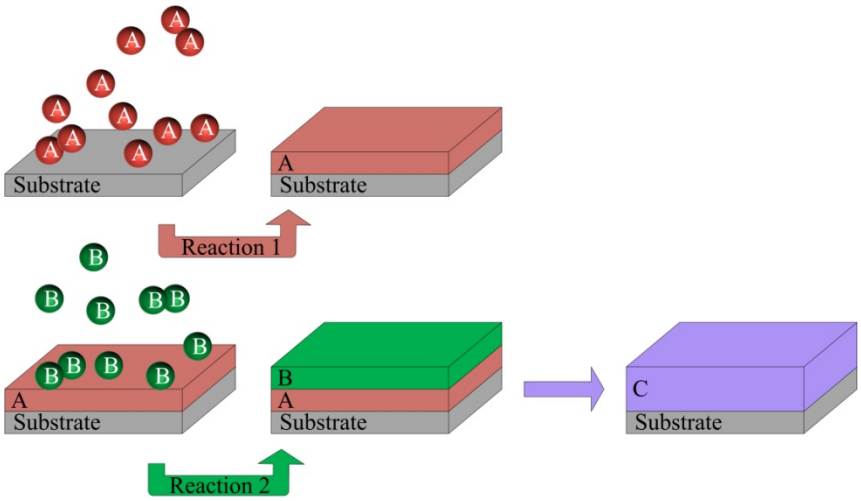


Figure 3.14 Schematic concept of ALD process.

Atomic Layer Deposition (ALD) is a gas phase deposition method for ultra-thin films [88]. Comparing to other deposition techniques, ALD has many advantages, such as excellent conformal and uniform coating on a very large area, as well as thickness and composition control at atomic level. ALD is based on self-limiting surface reactions.

During ALD process, two (or more) precursors are pulsed onto the substrate alternatively, and the pulses are separated by purges with an inert gas. Generally, *a-b-c-d* is referred as one cycle, where *a* is the pulse time of the first precursor, *c* is that of the second precursor, *b* and *d* indicate the purging period of inert gas after each pulse of precursor. In each cycle, a series of saturative reactions happen on the substrate surface and an atomic layer of target material is formed, described in Figure 3.14. This self-limiting growth is the key feature for ALD. During each cycle, gaseous precursor reacts with the solid substrate surface. Atoms which are included in the target material are absorbed to the substrate surface until the amount of atoms saturate. Simultaneously, atoms which are not included in the target material are removed as reaction byproducts [89]. Thus, as the number of cycles is determined, the target material with accurate thickness should be expected. Figure 3.15 shows a SEM photo of a ~ 50 nm layer of $HfO_2$ deposited by ALD on Si substrate.

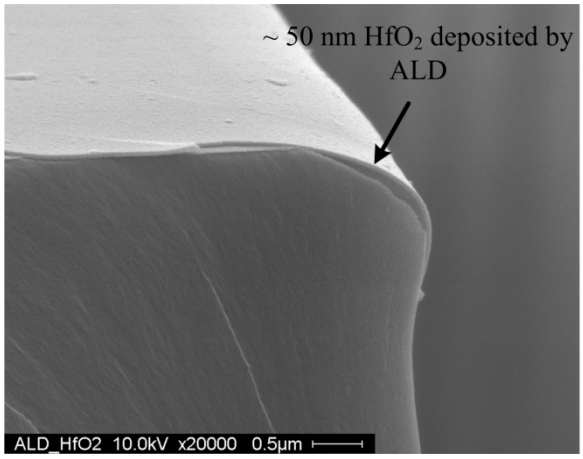


Figure 3.15 SEM image of a thin film of $HfO_2$ of ~ 50 nm deposited by ALD on Si substrate.

Table 3.2 summarizes the precursors and deposition rate at different temperatures of $HfO_2$, showing that deposition rate increases as deposition temperature decreases.

Table 3.2 Precursors, deposition condition and rate of $HfO_2$ deposited by ALD.

| Deposition condition | | Flow rate (sccm) | Pulse $H_2O$ (s) | Wait (s) | Pulse $Hf(NMe_2)_4$ (s) | Wait (s) | Deposition rate (Å/cycle) |
|---|---|---|---|---|---|---|---|
| Temperature ($^oC$) | 150 | 20 | 0.015 | 60 | 0.15 | 60 | 1.0523 |
| | 200 | 20 | 0.015 | 25 | 0.1 | 25 | 0.9012 |
| | 250 | 20 | 0.03 | 5 | 0.3 | 5 | 0.8444 |

In order to protect the high-k dielectric material deposited by ALD in the $SiO_2$ releasing process, thus enabling the optimized dielectric transducer, the etch rate in HF of $HfO_2$ film at different deposition temperature is then investigated. As-deposit $HfO_2$ film is etched in 50:1 HF and the film deposited at lower temperature showed lower etch rate, thus higher resistivity to HF, as illustrated in Figure 3.16. $HfO_2$ film is then annealed at 800$^o$C for 5 minutes in a tube furnace with an $N_2$ ambient at atmospheric pressure and etched in 49% pure HF. Etch rate of annealed $HfO_2$ film in HF drops dramatically, which is almost zero in pure HF. Thickness of $HfO_2$ films is measured by Rudolph ellipsometer with reflective index of 2.05.

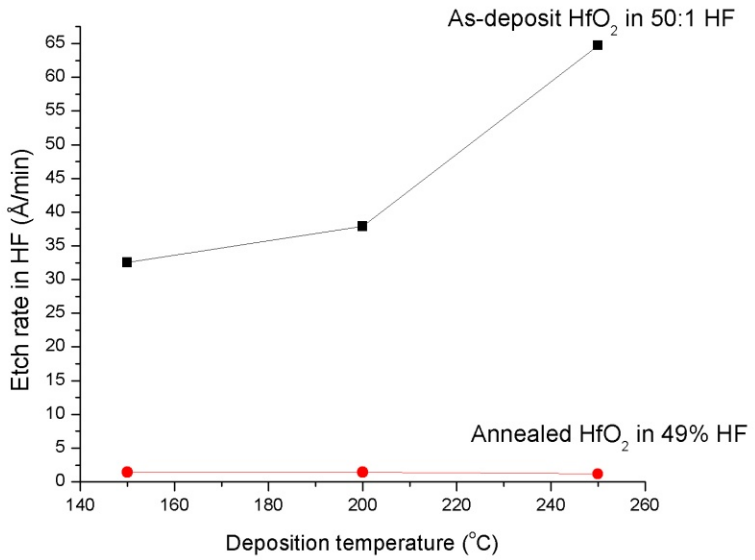


Figure 3.16 Etch rate in HF of $HfO_2$ deposited at different temperature and with different post-deposition treatment.

In addition, grazing incidence x-ray diffraction (GI-XRD) measurement obtained by Philips PW3040 X'pert PRO system indicates that not only the deposition rate, crystal structure of these materials also depends on the deposition temperature and annealing treatments, as demonstrated in Figure 3.17. XRD patterns show that all peaks grow dramatically when ALD $HfO_2$ films are annealed, suggesting a much better crystallized film is obtained after annealing. Moreover, as deposition temperature decreases, all monoclinic peaks (i.e., oriented in (110), (200), and (201)) grow in intensity while the peak near $2\theta = 30.4^{o}$ does not, which corresponds to either a tetragonal or orthorhombic phase. This observation suggested that the tetragonal or orthorhombic phase is preferred in higher deposition temperature.

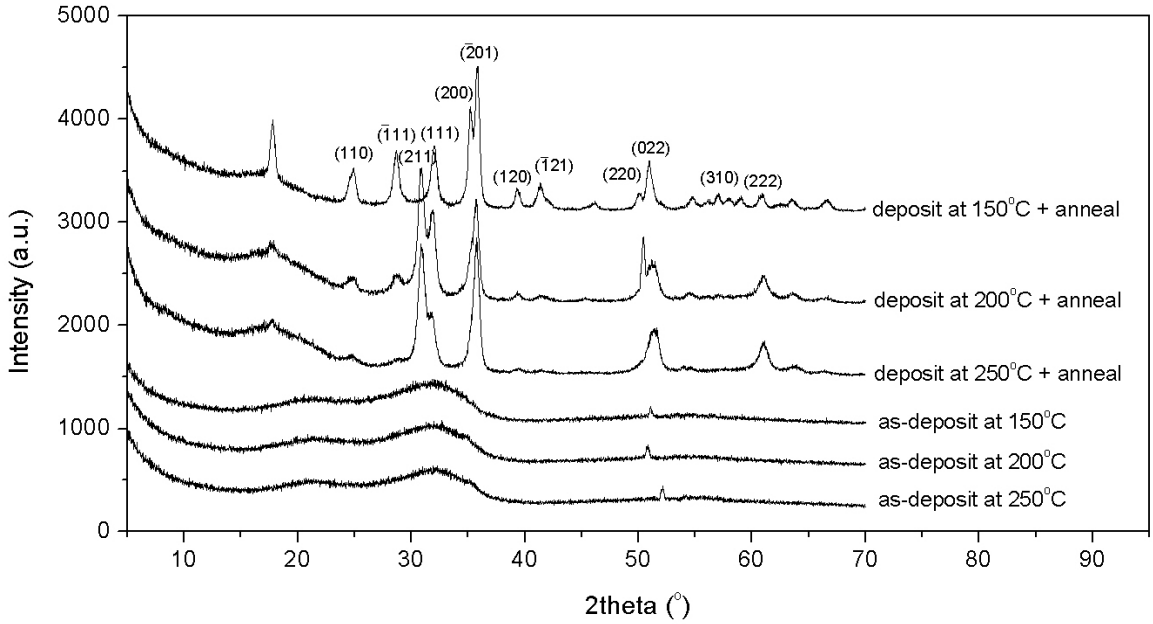


Figure 3.17 XRD spectra of ALD $HfO_2$ films on thermal oxide underlayer showing the effect of deposition temperature and annealing.

ALD $HfO_2$ film is served as a high-k dielectric solid gap in the capacitively-transduced resonator, thus making the dielectric constant a crucial property of the film.

High frequency (HF) Capacitance-Voltage (C-V) measurements are performed on the as-deposit and $N_2$ annealed ALD $HfO_2$ films with a deposition temperature of 150°C. Aluminum top circular electrodes with diameter of 1 mm are deposited by an e-beam evaporator through a shadow mask and HP 4145B was used for C-V measurements.

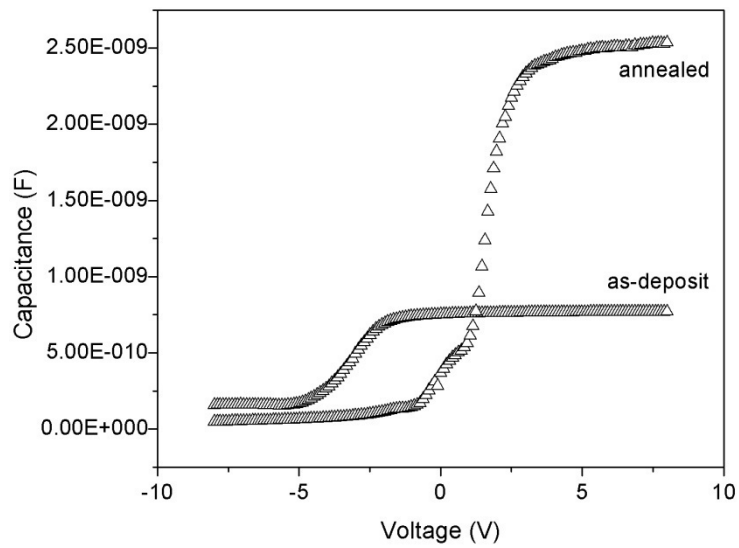


Figure 3.18 HF C-V measurement of a MOS capacitor with ALD $HfO_2$ film as dielectric.

As shown in Figure 3.18, the capacitance of the ALD $HfO_2$ film increases from 800 pF to 2.5 nF after annealing. With an assumption that the capacitance of the $HfO_2$ film equals to accumulation capacitance, the dielectric constant can be calculated as

$$\varepsilon_{r,HfO_2} = \frac{C_{ox} \cdot d}{\varepsilon_0 \cdot A}, \qquad 3.3$$

where $C_{ox}$ is the capacitance of the dielectric layer, $d$ is the thickness of the $HfO_2$ film, $A$ is the area of the aluminum electrode, and $\varepsilon_0$ is the dielectric constant of a free space. Hence, the calculated dielectric constant of the ALD $HfO_2$ film deposited at 150°C is 6.06 and 15.66 for as-deposit and annealed film, respectively, suggesting that annealed $HfO_2$ is preferred in this process not only because of its high resistivity to HF solution but also because of its much higher dielectric constant.

# CHAPTER 4 CONCLUSION

Due to the high-$Q$ and CAD-layout definable ultrahigh resonance frequencies, MEMS resonators offer a promising on-chip replacement to eliminate the board-level RF passives, thus leading to ultimate miniaturization and performance improvement. In particular, the future transceiver architecture can benefit from large arrays of micromechanical resonator filters, because of their tiny sizes and low power consumption, and possibility for multiband selection. It is beyond doubt that researches on MEMS devices for wireless communication on device and system level still have a boarder space to develop and will make influence in the near future.

However, the excessive motional impedance has impeded further development of the capacitively-transduced MEMS resonators. Motional impedance is a function of several parameters, including the disk-to-electrode overlap area, gap distance of the dielectric, and dielectric constant of the gap material. SOI technique provides a promising approach to greatly enhance the overlap area thus reduce the motional impedance, while offering better mechanical and thermal characteristics of single crystal silicon comparing to conventionally used polycrystalline silicon. Therefore, this work is preceded for the purpose of designing a novel fabrication process of capacitively-transduced MEMS resonators and resonator arrays on SOI substrate, which can be CMOS compatible and much easier to realize than currently available processes.

Bosch process is used to etch the device Si layer of a SOI wafer in order to define the resonator body structure. Insight investigation has been performed for the purposes of

optimizing Si etch rate, Si trench sidewall smoothness and profile. The optimized parameters, including gas pulse time, flow rate, power, and post-etching surface treatment, are experimentally demonstrated in this work.

The solid capacitive gap is deposited by ALD, and high-k dielectric materials are chosen. The dielectric constant of these high-k materials under different deposition conditions and different post-deposition treatments has been studied.

## LIST OF REFERENCES


[1] P. V. David Tse, *Fundamentals of Wireless Communication*: Cambridge University Press, 2005.

[2] T. P. Liu and E. Westerwick, "5-GHz CMOS radio transceiver front-end chipset," *Ieee Journal of Solid-State Circuits,* vol. 35, pp. 1927-1933, 2000.

[3] S.-J. C. a. Y.-H. Hsieh, "Transceiver Arechitecture Design," in *IQ Calibration Techniques for CMOS Radio Transceivers*: Springer Netherlands, 2006, pp. 11-42.

[4] M. Brandolini, P. Rossi, D. Manstretta, and F. Svelto, "Toward multistandard mobile terminals - Fully integrated receivers requirements and architectures," *Ieee Transactions on Microwave Theory and Techniques,* vol. 53, pp. 1026-1038, 2005.

[5] D. Jakonis, K. Folkesson, J. Dabrowski, P. Eriksson, and C. Svensson, "A 2.4-GHz RF sampling receiver front-end in 0.18-mu m CMOS," *Ieee Journal of Solid-State Circuits,* vol. 40, pp. 1265-1277, 2005.

[6] C. T. C. Nguyen, "Transceiver front-end architectures using vibrating micromechanical signal processors," *Rf Technologies for Low Power Wireless Communications,* pp. 411-461, 2001.

[7] J. Wang, J. E. Butler, T. Feygelson, and C. T. C. Nguyen, "1.51-GHz nanocrystalline diamond micromechanical disk resonator with material-mismatched isolating support," in *IEEE International Conference on. (MEMS)*, 2004, pp. 641-644.

[8] Y. Xie, S. S. Li, Y. W. Lin, Z. Y. Ren, and C. T. C. Nguyen, "1.52-GHz micromechanical extensional wine-glass-mode ring resonators," *IEEE Transactions on Ultrasonics Ferroelectrics and Frequency Control,* vol. 55, pp. 890-907, 2008.

[9] J. Wang, Z. Y. Ren, and C. T. C. Nguyen, "1.156-GHz self-aligned vibrating micromechanical disk resonator," *IEEE Transactions on Ultrasonics Ferroelectrics and Frequency Control,* vol. 51, pp. 1607-1628, 2004.

[10] D. Weinstein, S. A. Bhave, S. Morita, S. Mitarai, and K. Ikeda, "Frequency scaling and transducer efficiency in internal dielectrically transduced silicon bar resonators," in *Solid-State Sensors, Actuators and Microsystems Conference, 2009. TRANSDUCERS 2009. International*, 2009, pp. 708-711.

[11] D. Weinstein and S. A. Bhave, "Internal Dielectric Transduction of a 4.5 GHz Silicon Bar Resonator," in *IEEE International Electron Devices Meeting*, 2007, pp. 415-418.

[12] H. Wan-Thai and C. T. C. Nguyen, "Stiffness-compensated temperature-insensitive micromechanical resonators," in *Micro Electro Mechanical Systems, 2002. The Fifteenth IEEE International Conference on*, 2002, pp. 731-734.

[13] M. A. Hopcroft, H. K. Lee, B. Kim, R. Melamud, S. Chandorkar, M. Agarwal, C. Jha, J. Salvia, G. Bahl, H. Mehta, and T. W. Kenny, "A High-Stability MEMS Frequency Reference," in *Solid-State Sensors, Actuators and Microsystems Conference, 2007. TRANSDUCERS 2007. International*, 2007, pp. 1307-1309.

[14] C. Kuan-Lin, S. Wang, J. Salvia, R. T. Howe, and T. W. Kenny, "Encapsulated out-of-plane differential square-plate resonator with integrated actuation electrodes," in *Solid-State Sensors, Actuators and Microsystems Conference, 2009. TRANSDUCERS 2009. International*, 2009, pp. 1421-1424.

[15] S.-S. Li, Y.-W. Lin, Z. Ren, and C. T. C. Nguyen, "Self-switching vibrating micromechanical filter bank," in *Frequency Control Symposium and Exposition, 2005. Proceedings of the 2005 IEEE International*, 2005, p. 7 pp.

[16] H. Nakahata, H. Kitabayashi, T. Uemura, A. Hachigo, K. Higaki, S. Fujii, Y. Seki, K. Yoshida, and S. Shikata, "Study on surface acoustic wave characteristics of SiO2/interdigital-transducer/ZnO/diamond structure and fabrication of 2.5 GHz narrow band filter," *Japanese Journal of Applied Physics Part 1-Regular Papers Brief Communications & Review Papers,* vol. 37, pp. 2918-2922, 1998.

[17] A. Gaidarzhy, M. Imboden, P. Mohanty, J. Rankin, and B. W. Sheldon, "High quality factor gigahertz frequencies in nanomechanical diamond resonators," *Applied Physics Letters,* vol. 91, 2007.

[18] N. Kacem, S. Hentz, D. Pinto, B. Reig, and V. Nguyen, "Nonlinear dynamics of nanomechanical beam resonators: improving the performance of NEMS-based sensors," *Nanotechnology,* vol. 20, 2009.

[19] S. B. Cohn, "Microwave Bandpass Filters Containing High-Q Dielectric Resonators," *IEEE Transactions on Microwave Theory and Techniques,* vol. 16, pp. 218-227, 1968.

[20] S. J. Fiedziuszko, I. C. Hunter, T. Itoh, Y. Kobayashi, T. Nishikawa, S. N. Stitzer, and K. Wakino, "Dielectric materials, devices, and circuits," *IEEE Transactions on Microwave Theory and Techniques,* vol. 50, pp. 706-720, 2002.

[21] J. K. Plourde and C. L. Ren, "Application of dielectric resonators in microwave components," *IEEE Transactions on Microwave Theory and Techniques,* vol. 29, pp. 754-770, 1981.

[22] R. D. Richtmyer, "Dielectric resonators," *Journal of Applied Physics,* vol. 10, pp. 391-398, 1939.

[23] J. Viennet, M. Jardino, R. Barillet, and M. Desaintfuscien, "Frequency control loop with digital integrator," *IEEE Transactions on Instrumentation and Measurement,* vol. 32, pp. 322-326, 1983.

[24] A. S. Matistic, "Quartz-crystal timing accuracy is hard to beat," *Electronic Design|Electronic Design,* vol. 24, pp. 74-9, 1976.

[25] T. Ormond, "Crystal-oscillators-signal sources handle tough timing jobs," *Edn,* vol. 35, p. 93, 1990.

[26] W. P. Mason, "Electrical wave filters employing quartz crystals as elements," *Bell System Technical Journal,* vol. 13, pp. 405-452, 1934.

[27] P. Lloyd, "Monolithic crystal filters," *Proceedings of the 7th international congress on acoustics|Proceedings of the 7th international congress on acoustics,* pp. 309-12|xvi+568, 1971.

[28] C. P. Yue and S. S. Wong, "On-chip Spiral Inductors With Patterned Ground Shields For Si-based RF IC's," in *VLSI Circuits, 1997. Digest of Technical Papers., 1997 Symposium on*, 1997, pp. 85-86.

[29] X. M. H. Huang, C. A. Zorman, M. Mehregany, and M. L. Roukes, "Nanodevice motion at microwave frequencies," *Nature,* vol. 421, pp. 496-496, 2003.

[30] D. Weinstein and S. A. Bhave, "The Resonant Body Transistor," *Nano Letters,* 2010.

[31] J. R. Vig and Y. Kim, "Noise in microelectromechanical system resonators," *IEEE Transactions on Ultrasonics Ferroelectrics and Frequency Control,* vol. 46, pp. 1558-1565, 1999.

[32] Y. Satoh, T. Nishihara, T. Yokoyama, M. Ueda, and T. Miyashita, "Development of piezoelectric thin film resonator and its impact on future wireless communication systems," *Japanese Journal of Applied Physics Part 1-Regular Papers Brief Communications & Review Papers,* vol. 44, pp. 2883-2894, 2005.

[33] D. P. Morgan, "History of saw devices," *Proceedings of the 1998 Ieee International Frequency Control Symposium,* pp. 439-460, 1998.

[34] Z. Hao and K. Eun Sok, "Air-backed Al/ZnO/Al film bulk acoustic resonator without any support layer," in *Frequency Control Symposium and PDA Exhibition, 2002. IEEE International*, 2002, pp. 20-26.

[35] K. Umeda, H. Kawamura, M. Takeuchi, and Y. Yoshino, "Characteristics of an AlN-based bulk acoustic wave resonator in the super high frequency range," *Vacuum,* vol. 83, pp. 672-674, 2008.

[36] J. B. Lee, H. J. Kim, S. G. Kim, C. S. Hwang, S. H. Hong, Y. H. Shin, and N. H. Lee, "Deposition of ZnO thin films by magnetron sputtering for a film bulk acoustic resonator," *Thin Solid Films,* vol. 435, pp. 179-185, 2003.

[37] M. A. Dubois and P. Muralt, "Properties of aluminum nitride thin films for piezoelectric transducers and microwave filter applications," *Applied Physics Letters,* vol. 74, pp. 3032-3034, 1999.

[38] K. M. Lakin, G. R. Kline, and K. T. McCarron, "Development of miniature filters for wireless applications," *IEEE Transactions on Microwave Theory and Techniques,* vol. 43, pp. 2933-2939, 1995.

[39] G. Piazza, P. J. Stephanou, and A. P. Pisano, "One and two port piezoelectric higher order contour-mode MEMS resonators for mechanical signal processing," *Solid-State Electronics,* vol. 51, pp. 1596-1608, 2007.

[40] G. Piazza, P. J. Stephanou, and A. P. Pisano, "Single-chip multiple-frequency ALN MEMS filters based on contour-mode piezoelectric resonators," *Journal of Microelectromechanical Systems,* vol. 16, pp. 319-328, 2007.

[41] R. H. Olsson, K. E. Wojciechowski, M. S. Baker, M. R. Tuck, and J. G. Fleming, "Post-CMOS-Compatible Aluminum Nitride Resonant MEMS Accelerometers," *Journal of Microelectromechanical Systems,* vol. 18, pp. 671-678, 2009.

[42] G. Piazza, P. J. Stephanou, and A. P. Pisano, "Piezoelectric aluminum nitride vibrating contour-mode MEMS resonators," *Journal of Microelectromechanical Systems,* vol. 15, pp. 1406-1418, 2006.

[43] C. T. C. Nguyen, "MEMS technology for timing and frequency control," *Ieee Transactions on Ultrasonics Ferroelectrics and Frequency Control,* vol. 54, pp. 251-270, 2007.

[44] R. Raiteri, M. Grattarola, H.-J. Butt, and P. Skládal, "Micromechanical cantilever-based biosensors," *Sensors and Actuators B: Chemical,* vol. 79, pp. 115-126, 2001.

[45] Y. W. Lin, S. Lee, S. S. Li, Y. Xie, Z. Y. Ren, and C. T. C. Nguyen, "Series-resonant VHF micromechanical resonator reference oscillators," *Ieee Journal of Solid-State Circuits,* vol. 39, pp. 2477-2491, 2004.

[46] F. D. Bannon, J. R. Clark, and C. T. C. Nguyen, "High-Q HF microelectromechanical filters," *IEEE Journal of Solid-State Circuits,* vol. 35, pp. 512-526, 2000.

[47] K. Wang, A. C. Wong, and C. T. C. Nguyen, "VHF free-free beam high-Q micromechanical resonators," *Journal of Microelectromechanical Systems,* vol. 9, pp. 347-360, 2000.

[48] A. N. Cleland and M. L. Roukes, "Fabrication of high frequency nanometer scale mechanical resonators from bulk Si crystals," *Applied Physics Letters,* vol. 69, pp. 2653-2655, 1996.

[49] W. Jing, R. Zeying, and C. T. C. Nguyen, "Self-aligned 1.14-GHz vibrating radial-mode disk resonators," in *TRANSDUCERS, Solid-State Sensors, Actuators and Microsystems, 12th International Conference on, 2003*, 2003, pp. 947-950 vol.2.

[50] J. R. Clark, H. Wan-Thai, and C. T. C. Nguyen, "High-Q VHF micromechanical contour-mode disk resonators," in *Electron Devices Meeting, 2000. IEDM Technical Digest. International*, 2000, pp. 493-496.

[51] M. A. Abdelmoneum, M. U. Demirci, and C. T. C. Nguyen, "Stemless wine-glass-mode disk micromechanical resonators," in *Micro Electro Mechanical Systems, 2003. MEMS-03 Kyoto. IEEE The Sixteenth Annual International Conference on*, 2003, pp. 698-701.

[52] W. Jing, Z. Y. Ren, and C. T. C. Nguyen, "1.156-GHz self-aligned vibrating micromechanical disk resonator," *Ieee Transactions on Ultrasonics Ferroelectrics and Frequency Control,* vol. 51, pp. 1607-1628, 2004.

[53] L. Sheng-Shian, L. Yu-Wei, X. Yuan, R. Zeying, and C. T. C. Nguyen, "Micromechanical "hollow-disk" ring resonators," in *Micro Electro Mechanical Systems, 2004. 17th IEEE International Conference on. (MEMS)*, 2004, pp. 821-824.

[54] T. J. Cheng, Bhave, S. A. , "High-Q, low impedance polysilicon resonators with 10 nm air gaps," in *IEEE International Conference on Micro Electro Mechanical Systems*, 2010, pp. 695-698.

[55] S. Pourkamali, Z. Hao, and F. Ayazi, "VHF single crystal silicon capacitive elliptic bulk-mode disk resonators - Part II: Implementation and characterization," *Journal of Microelectromechanical Systems,* vol. 13, pp. 1054-1062, 2004.

[56] V. T. Srikar and S. D. Senturia, "Thermoelastic damping in fine-grained polysilicon flexural beam resonators," *Journal of Microelectromechanical Systems,* vol. 11, pp. 499-504, 2002.

[57] K. Y. Yasumura, T. D. Stowe, E. M. Chow, T. Pfafman, T. W. Kenny, B. C. Stipe, and D. Rugar, "Quality factors in micron- and submicron-thick cantilevers," *Journal of Microelectromechanical Systems,* vol. 9, pp. 117-125, 2000.

[58] M. Bruel, "Silicon on insulator material technology," *Electronics Letters,* vol. 31, pp. 1201-1202, 1995.

[59] Y. Taur, D. A. Buchanan, W. Chen, D. J. Frank, K. E. Ismail, S. H. Lo, G. A. SaiHalasz, R. G. Viswanathan, H. J. C. Wann, S. J. Wind, and H. S. Wong, "CMOS scaling into the nanometer regime," *Proceedings of the Ieee,* vol. 85, pp. 486-504, 1997.

[60] D. W. Carr and H. G. Craighead, "Fabrication of nanoelectromechanical systems in single crystal silicon using silicon on insulator substrates and electron beam lithography," *Journal of Vacuum Science & Technology B,* vol. 15, pp. 2760-2763, 1997.

[61] L. A. Giannuzzi and F. A. Stevie, "A review of focused ion beam milling techniques for TEM specimen preparation," *Micron,* vol. 30, pp. 197-204, 1999.

[62] D. Grogg, N. D. Badila-Ciressan, and A. M. Ionescu, "Focussed ion beam based fabrication of micro-electro-mechanical resonators," *Microsystem Technologies-Micro-and Nanosystems-Information Storage and Processing Systems,* vol. 14, pp. 1049-1053, 2008.

[63] S. Pourkamali and F. Ayazi, "SOI-based HF and VHF single-crystal silicon resonators with SUB-100 nanometer vertical capacitive gaps," in *TRANSDUCERS, Solid-State Sensors, Actuators and Microsystems, 12th International Conference on, 2003*, 2003, pp. 837-840 vol.1.

[64] Z. Hao, S. Pourkamali, and F. Ayazi, "VHF single-crystal silicon elliptic bulk-mode capacitive disk resonators - Part I: Design and modeling," *Journal of Microelectromechanical Systems,* vol. 13, pp. 1043-1053, 2004.

[65] C. Nicoleta Diana Badila, H. Cyrille, M. Marco, and M. I. Adrian, "Fabrication of silicon-on-insulator MEM resonators with deep sub-micron transduction gaps," *Microsyst. Technol.,* vol. 13, pp. 1489-1493, 2007.

[66] D. Grogg, H. C. Tekin, N. D. Ciressan-Badila, D. Tsamados, M. Mazza, and A. M. Ionescu, "Bulk Lateral MEM Resonator on Thin SOI With High Q-Factor," *Microelectromechanical Systems, Journal of,* vol. 18, pp. 466-479, 2009.

[67] M. U. Demirci, M. A. Abdelmoneum, and C. T. C. Nguyen, "Mechanically corner-coupled square microresonator array for reduced series motional resistance," in *TRANSDUCERS, Solid-State Sensors, Actuators and Microsystems, 12th International Conference on, 2003*, 2003, pp. 955-958 vol.2.

[68] W. Jing, J. E. Butler, T. Feygelson, and C. T. C. Nguyen, "1.51-GHz nanocrystalline diamond micromechanical disk resonator with material-mismatched isolating support," in *IEEE International Conference on. (MEMS)*, 2004, pp. 641-644.

[69] N. Sepulveda, L. Jing, D. M. Aslam, and J. P. Sullivan, "High-Performance Polycrystalline Diamond Micro- and Nanoresonators," *Microelectromechanical Systems, Journal of,* vol. 17, pp. 473-482, 2008.

[70] V. P. Adiga, A. V. Sumant, S. Suresh, C. Gudeman, O. Auciello, J. A. Carlisle, and R. W. Carpick, "Mechanical stiffness and dissipation in ultrananocrystalline diamond microresonators," *Physical Review B,* vol. 79, 2009.

[71] A. R. Krauss, O. Auciello, D. M. Gruen, A. Jayatissa, A. Sumant, J. Tucek, D. C. Mancini, N. Moldovan, A. Erdemir, D. Ersoy, M. N. Gardos, H. G. Busmann, E. M. Meyer, and M. Q. Ding, "Ultrananocrystalline diamond thin films for MEMS and moving mechanical assembly devices," *Diamond and Related Materials,* vol. 10, pp. 1952-1961, 2001.

[72] C. Förster, V. Cimalla, V. Lebedev, J. Pezoldt, K. Brueckner, R. Stephan, M. Hein, E. Aperathitis, and O. Ambacher, "Group III-nitride and SiC based micro- and nanoelectromechanical resonators for sensor applications," *physica status solidi (a),* vol. 203, pp. 1829-1833, 2006.

[73] J. R. Clark, W. T. Hsu, M. A. Abdelmoneum, and C. T. C. Nguyen, "High-Q UHF micromechanical radial-contour mode disk resonators," *Microelectromechanical Systems, Journal of,* vol. 14, pp. 1298-1310, 2005.

[74] D. J. Young, I. E. Pehlivanoglu, and C. A. Zorman, "Silicon carbide MEMS-resonator-based oscillator," *Journal of Micromechanics and Microengineering,* vol. 19, 2009.

[75] H. Wen-Lung, L. Sheng-Shian, R. Zeying, and C. T. C. Nguyen, "UHF Nickelmicromechanical Spoke-Supported Ring Resonators," in *Solid-State Sensors, Actuators and Microsystems Conference, 2007. TRANSDUCERS 2007. International*, 2007, pp. 323-326.

[76] H. Wen-Lung, R. Zeying, L. Yu-Wei, C. Hsien-Yeh, J. Lahann, and C. T. C. Nguyen, "Fully monolithic CMOS nickel micromechanical resonator oscillator," in *Micro Electro Mechanical Systems, 2008. MEMS 2008. IEEE 21st International Conference on*, 2008, pp. 10-13.

[77] A. E. H. Love, *A treatise on the mathematical theory of elasticity*: University Press (Cambridge), 1906.

[78] S. H. C. Stanley and L. Ta Ming, "Extensional vibration of thin plates of various shapes," *The Journal of the Acoustical Society of America,* vol. 58, pp. 828-831, 1975.

[79] N. H. Farag and J. Pan, "Modal characteristics of in-plane vibration of circular plates clamped at the outer edge," *The Journal of the Acoustical Society of America,* vol. 113, pp. 1935-1946, 2003.

[80] M. Onoe, "Contour Vibrations of Isotropic Circular Plates," *The Journal of the Acoustical Society of America,* vol. 28, pp. 1158-1162, 1956.

[81] T. Takano, H. Hirata, and Y. Tomikawa, "Analysis of nonaxisymmetric vibration mode piezoelectric annular plate and tis application to an ultrasonic motor," *IEEE Transactions on Ultrasonics Ferroelectrics and Frequency Control,* vol. 37, pp. 558-565, 1990.

[82] D. M. Pozar, *Microwave Engineering*, 2nd ed.: WILEY, 1998.

[83] D. L. DeVoe, "Piezoelectric thin film micromechanical beam resonators," *Sensors and Actuators A: Physical,* vol. 88, pp. 263-272, 2001.

[84] C. L. Chang, Y. F. Wang, Y. Kanamori, J. J. Shih, Y. Kawai, C. K. Lee, K. C. Wu, and M. Esashi, "Etching submicrometer trenches by using the Bosch process and its application to the fabrication of antireflection structures," *Journal of Micromechanics and Microengineering,* vol. 15, pp. 580-585, 2005.

[85] A. Sharma, F. M. Zaman, B. V. Amini, and F. Ayazi, "A high-Q in-plane SOI tuning fork gyroscope," in *Sensors, 2004. Proceedings of IEEE*, 2004, pp. 467-470 vol.1.

[86] B. V. Amini, R. Abdolvand, and F. Ayazi, "Sub-micro-gravity capacitive SOI microaccelerometers," in *Solid-State Sensors, Actuators and Microsystems, 2005. Digest of Technical Papers. TRANSDUCERS '05. The 13th International Conference on*, 2005, pp. 515-518 Vol. 1.

[87] S. Pourkamali, G. K. Ho, and F. Ayazi, "Vertical capacitive SiBARs," in *Micro Electro Mechanical Systems, 2005. MEMS 2005. 18th IEEE International Conference on*, 2005, pp. 211-214.

[88] M. Leskelä and M. Ritala, "Atomic layer deposition (ALD): from precursors to thin film structures," *Thin Solid Films,* vol. 409, pp. 138-146, 2002.

[89] R. L. Puurunen, "Surface chemistry of atomic layer deposition: A case study for the trimethylaluminum/water process," *Journal of Applied Physics,* vol. 97, pp. 121301-52, 2005.

# APPENDICES

## Appendix A: Polysilicon Disk Resonator on SOI Substrate Process Traveler

A.1 Deposit Isolation Layers

A.1.1 Thermally grow 2 um $SiO_2$ on SOI substrate

Equipment: FNB2

A.2 Pattern Resonator Body Structure (Mask 1)

A.2.1 Lithography AZ4620 ~5.0 um

Dehydration bake: 5 min @ 150°C

Spin: Laura Spinner

HMDS: 20 sec @ 1500 RPM

AZ4620: 20 sec @ 1500 RPM

50 sec @ 4000 RPM

10 sec @ 6000 RPM

Softbake: 5 min @ 100°C

Exposure: 5 sec @ 25 mW/cm$^2$, vacuum contact

Develop: 4 min in diluted (4:1) AZ 400K

A.2.2 Descum

Equipment: Plasma Therm

$O_2$: 50 sccm

Pressure: 300 mTorr

Power: 100 watts

Time: 10 min

A.2.3 $SiO_2$ DRIE

Equipment: Alcatel AMS 100

**Appendix A (Continued)**

C4F8: 17 sccm

He: 150 sccm

$CH_4$: 13 sccm

Power: 2800 watts

Time: 1.5 min

$O_2$ chamber clean: 1.5 min

A.2.4 Si DRIE

Equipment: AMS 100, Alcatel Vacuum Technology, France

$SF_6$: 300 sccm, 3 sec

$C_4F_8$: 200 sccm; $O_2$: 20 sccm, 1.4 sec

Power: 2400 watts

Pulsed power: 25 ms @ 100 watts; 75 ms @ 0 watts

Substrate temperature: -15 °C

Time: 4 min

Etch rate: ~0.8 um/min

$O_2$ chamber clean: 5 min

A.3 Deposit and Anneal Dielectric layer ($HfO_2$)

A.3.1 Deposit $HfO_2$ by Atomic Layer Deposition (ALD) ~ 20 nm

Equipment: Savannah, Cambridge NanoTech Inc. , USA

Temperature: I=O=200 °C, T=V=B=150 °C

Flow rate: 20 sccm

Recipe: pulse $H_2O$, 0.015 sec

**Appendix A (Continued)**

wait 25 sec

pulse $Hf(NMe_2)_4$, 0.1 sec

wait 25 sec

cycle 220

Deposition rate: 0.9 Å/cycle

A.3.2 $HfO_2$ Anneal

Equipment: tube furnace

Temperature: 800 °C

Gas: $N_2$

Time: 5 min

A.4 Deposit and Dope Poly-Si Layer

A.4.1 Deposit poly-Si by Low Pressure Chemical Vapor Deposition (LPCVD) ~2 um

Equipment: FNB 4

Program: Z9641

Temperature: 605 °C

Time: 290 min

Deposition rate: ~70 Å/min

A.4.1 Dope poly-Si using solid source

Equipment: FNB 3

Solid source: BN1050, Saint-Gobain Ceramics & Plastics, Inc., USA

A.4.1.1 Predeposition

**Appendix A (Continued)**

Program: M4007

Temperature: 1050 °C

Time: 30 min

A.4.1.2 Drive-in

Program: M4008

Temperature: 1050 °C

Time: 30 min

A.4.1.3 Deglaze

20 min in 6:1 BOE

A.4.1.4 Low temperature dry oxidation

Program: M4005

Temperature: 900 °C

Time: 20 min

A.4.1.5 Deglaze

20 ~ 50 min in 6:1 BOE until the surface become hydrophilic

A.4.1.6 Sheet resistance measurement ~ 20 Ohm/sq

Equipment: four-point probe

A.5 Pattern Poly-Si Electrodes (Mask 2)

A.5.1 Lithography SU-8 3025 ~ 50 um

Dehydration bake: 5 min @ 150 °C

Spin: Laura Spinner

10 sec @ 500 RPM

**Appendix A (Continued)**

40 sec @ 2000 RPM

Soft bake: 12 min @ 95 °C

Exposure: 20 sec @ 25 mW/cm2, hard contact, with high-wavelength pass filter

Post exposure bake: 1 min @ 65 °C; 4 min @ 95 °C

Develop: 8 min in SU-8 developer

A.5.2 Descum

Equipment: Plasma Therm

$O_2$: 50 sccm

Pressure: 300 mTorr

Power: 100 watts

Time: 10 min

A.5.3 Poly-Si RIE

Equipment: Plasma Therm

$SF_6$: 50 sccm

Pressure: 100 mTorr

Power: 100 watts

Time: 4 min

A.6 Pattern Opens to Substrate Contacts (Mask 3)

A.6.1 Lithography S1827 ~2.8 um

Equipment: Laura Spinner

Spin time: 30 sec @ 3500 RPM

**Appendix A (Continued)**

Softbake time: 1 min @ 115°C

Exposure time: 14 sec @ 25 mW

Develop time: 70 sec